



**HAL**  
open science

## Assessing the representation of tropical cyclones in ERA5 with the CNRM tracker

William Dulac, Julien Cattiaux, Fabrice Chauvin, Stella Bourdin, Sébastien Fromang

► **To cite this version:**

William Dulac, Julien Cattiaux, Fabrice Chauvin, Stella Bourdin, Sébastien Fromang. Assessing the representation of tropical cyclones in ERA5 with the CNRM tracker. *Climate Dynamics*, In press, 10.1007/s00382-023-06902-8 . hal-04180153v1

**HAL Id: hal-04180153**

**<https://hal.science/hal-04180153v1>**

Submitted on 11 Aug 2023 (v1), last revised 28 Nov 2023 (v2)

**HAL** is a multi-disciplinary open access archive for the deposit and dissemination of scientific research documents, whether they are published or not. The documents may come from teaching and research institutions in France or abroad, or from public or private research centers.

L'archive ouverte pluridisciplinaire **HAL**, est destinée au dépôt et à la diffusion de documents scientifiques de niveau recherche, publiés ou non, émanant des établissements d'enseignement et de recherche français ou étrangers, des laboratoires publics ou privés.



Distributed under a Creative Commons Attribution - NonCommercial 4.0 International License

## Assessing the representation of tropical cyclones in ERA5 with the CNRM tracker

This Accepted Manuscript (AM) is a PDF file of the manuscript accepted for publication after peer review, when applicable, but does not reflect post-acceptance improvements, or any corrections. Use of this AM is subject to the publisher's embargo period and AM terms of use. Under no circumstances may this AM be shared or distributed under a Creative Commons or other form of open access license, nor may it be reformatted or enhanced, whether by the Author or third parties. By using this AM (for example, by accessing or downloading) you agree to abide by Springer Nature's terms of use for AM versions of subscription articles: <https://www.springernature.com/gp/open-research/policies/accepted-manuscript-terms>

The Version of Record (VOR) of this article, as published and maintained by the publisher, is available online at: <https://doi.org/10.1007/s00382-023-06902-8>. The VOR is the version of the article after copy-editing and typesetting, and connected to open research data, open protocols, and open code where available. Any supplementary information can be found on the journal website, connected to the VOR.

For research integrity purposes it is best practice to cite the published Version of Record (VOR), where available (for example, see ICMJE's guidelines on overlapping publications). Where users do not have access to the VOR, any citation must clearly indicate that the reference is to an Accepted Manuscript (AM) version.

# Assessing the representation of tropical cyclones in ERA5 with the CNRM tracker

William Dulac<sup>1,2\*</sup>, Julien Cattiaux<sup>1</sup>, Fabrice  
Chauvin<sup>1</sup>, Stella Bourdin<sup>3</sup> and Sébastien Fromang<sup>3</sup>

<sup>1</sup>\*Centre National de Recherches Météorologiques (CNRM),  
Météo-France, Toulouse, France.

<sup>2</sup>Université Toulouse III - Paul Sabatier, Toulouse, France.

<sup>3</sup>Laboratoire des Sciences du Climat et de l'Environnement,  
LSCE/IPSL, CEA-CNRS-UVSQ-Université Paris-Saclay,  
Gif-sur-Yvette, France.

\*Corresponding author(s). E-mail(s): [william.dulac@meteo.fr](mailto:william.dulac@meteo.fr);

## Abstract

The ERA5 dataset from the European Center for Medium-Range Weather Forecasts is the first global reanalysis to reach a horizontal resolution of 31 km and thus provides a unique opportunity to look at tropical cyclones (TC), and in particular at the 3D fields associated with observed TCs. To that end, a specifically calibrated TC tracking scheme is applied on ERA5 along with a track pairing algorithm to match the detected tracks with the IBTrACS catalog in order to investigate how well TCs are represented in the reanalysis. After tuning of the tracking scheme and the application of a dynamic mid-latitude system filtering technique, it is shown that the majority of IBTrACS TCs are detected in ERA5 and that the amount of false alarms is kept reasonably low in most regions. By comparing detected tracks with their IBTrACS counterparts, it is found that TC intensity is still strongly underestimated in ERA5 but that the minimum sea-level pressure distribution is better represented than maximum wind speed. The comparison between the life cycles from both datasets highlights key differences between ERA5 and the best-track catalog, showing in particular that the delay with which TCs from ERA5 reach their peak intensity compared to IBTrACS increases significantly with real TC intensity increase. Finally,

2 *Assessing the representation of tropical cyclones in ERA5 with the CNRM tracker*

047 the internal structure of TCs in the reanalysis for each intensity class are  
048 analyzed and reveal distinct intensification patterns up to Category 3.

049 **Keywords:** Reanalysis, TC Tracking, Internal structure, Life cycle,  
050 Composites  
051

052  
053  
054

## 055 1 Introduction

056  
057

058 Atmospheric reanalyses have been developed continuously since [Kalnay et al](#)  
059 ([1996](#)) by a multitude of meteorological institutes throughout the world. While  
060 they have benefited from numerous technical improvements since then, the  
061 operating principle has remained unchanged: By combining past short-range  
062 weather forecasts with observations through an unchanging data assimila-  
063 tion scheme over the period being analyzed, reanalyses offer a physically and  
064 dynamically consistent global estimate of the state of the atmosphere at each  
065 time step. Such a product is of great value for the study of the atmospheric  
066 and climate system as it allows for direct comparison with the outputs from  
067 climate models. In fact, reanalyses are often used as reference for model eval-  
068 uation, in conjunction with direct observations ([Cesana et al, 2015](#); [Voldoire](#)  
069 [et al, 2019](#); [Fasullo, 2020](#)). Because of the good spatial and temporal homo-  
070 geneity they offer, reanalysis products are particularly useful for the study of  
071 tropical cyclones (TCs) at climate scales and can be used to circumvent the  
072 shortcomings of best-track catalogs ([Schreck et al, 2014](#)) caused in particular  
073 by differences in operational methodology among reporting agencies. But the  
074 major strength of atmospheric reanalysis for the study of TCs is that they offer  
075 the only mean of analyzing the internal 3D structure of present day TCs as  
076 well as the large scale environment around them. This is of utmost importance  
077 for the study of TCs in climate simulations. Reanalysis are therefore used to  
078 bridge the gap between observations and simulations for validating simulated  
079  
080  
081  
082  
083  
084  
085  
086  
087  
088  
089  
090  
091  
092

TCs (Murakami and Sugi, 2010; Bell et al, 2013; Rathmann et al, 2014). For that reason, the question of TC representation in reanalysis datasets is of great importance.

Yet, TCs in reanalysis suffer from coarse resolutions (Walsh et al, 2007) as well as from a lack of in-situ observations in certain areas. Consequently, some reanalyses have implemented TC-specific assimilation techniques to improve TC representation. Both the version 2 of the Modern-Era Retrospective Analysis for Research and Applications (MERRA-2, Gelaro et al, 2017) and the Climate Forecast System Reanalysis (CFSR, Saha et al, 2014) make use of a vortex relocation technique which consists in moving the position of the vortex closer to its best-track location or artificially inserting a vortex into the model's first-guess if absent or too weak. Reanalyses produced by the Japanese Meteorological Agency — namely the Japanese 25-year and 55-year Reanalyses (JRA-25, Onogi et al, 2007; Ebata et al, 2011, JRA-55) — retrieve wind profile data from best-track catalogs and assimilate them as dropwindsonde data (Hatsushika et al, 2006). Both these techniques have been shown to be beneficial to the placement of TC in reanalyses and for TC intensity (Schenkel and Hart, 2012; Murakami, 2014; Hodges et al, 2017).

ERA5 (Hersbach et al, 2020) is the fifth and latest atmospheric reanalysis from the European Center for Medium-Range Weather Forecasts (ECMWF), succeeding to ERA-Interim (Dee et al, 2011) and ERA-40 (Uppala et al, 2005). Currently extending from 1959 to the present day (still ongoing, and is planned to extend back to 1940), ERA5 uses a wide range of observations from satellite data to ground stations, instrumented buoys and reconnaissance aircraft data through the 4DVAR data assimilation scheme and produces hourly fields with a  $0.28125^\circ$  horizontal resolution and 137 vertical levels up to 0.01 hPa. The 4DVAR data assimilation scheme has been shown to perform better than

4 *Assessing the representation of tropical cyclones in ERA5 with the CNRM tracker*

139 3DVAR in areas where observations are sparse (Whitaker et al, 2009) and to  
140 have better predictive skill for TCs (Tiwari and Kumar, 2022). Lastly, The  
141 high resolution in ERA5 is also believed to improve TC representation com-  
142 pared to ERA-Interim (Hersbach et al, 2020). Additionally, the ERA5 back  
143 extension (BE) — covering the 1959 – 1978 period — assimilates IBTrACS  
144 6-hourly pressure reports to improve TC intensity (Bell et al, 2021). However,  
145 in a preliminary version of ERA5 BE, this unexpectedly resulted in some sys-  
146 tems being too intense, firstly because too much weight were inadvertently  
147 given to these observations during the production of ERA5 BE, and secondly  
148 because the assimilation system would sometimes move the pressure minimum  
149 away from the observation, resulting in a minimum deeper than the reported  
150 one. The issue has been addressed in the final revision of ERA5 BE. IBTrACS  
151 pressure reports were nevertheless not assimilated for the main product that  
152 starts from 1979 onwards, but the emergence of new sources of observations  
153 at that time (in-situ and satellites) is believed to compensate for this.

164 In this paper, we apply the CNRM TC Tracking Scheme (Chauvin et al,  
165 2006) to ERA5 to study TC representation in the reanalysis. First, we conduct  
166 a sensitivity analysis of our tracking scheme to its various detection thresholds  
167 by pairing detected tracks from the ERA5 to the IBTrACS historical best-  
168 track catalog in order to maximize the probability of detection while limiting  
169 the false alarm rate. With our tuned tracking scheme, we then focus on TCs  
170 that were successfully matched with IBTrACS and look at several of their  
171 characteristics including the wind-pressure relationship, comparative life cycles  
172 as well as composited internal structure. Section 2 describes the processing  
173 done on both ERA5 and IBTrACS, the TC tracking scheme as well as the track  
174 pairing algorithm. Section 3.1 presents the performances of the tuned tracking  
175 scheme over ERA5 while Sections 3.2, 3.3 and 3.4 present different aspects  
176  
177  
178  
179  
180  
181  
182  
183  
184

of the TC representation in the reanalysis. The tracking scheme's sensitivity 185  
analysis is presented in Appendix A. Lastly, Section 4 discusses the results and 186  
provides concluding thoughts. 187  
188

## 2 Data and Methods 191

### 2.1 Datasets 194

We use the ERA5 reanalysis from ECMWF with its native horizontal grid 196  
resolution of  $0.28125^\circ$  and interpolated to  $0.25^\circ$ . The CNRM tracking algo- 197  
rithm (Chauvin et al, 2006) is applied on ERA5 6-hourly fields to produce TC 198  
track data containing longitude/latitude coordinates, sea-level pressure, vor- 199  
ticity and maximum wind speed. NOAA's International Best Track Archive 200  
for Climate Stewardship (IBTrACS, Knapp et al (2010)) was then used as the 201  
reference dataset. IBTrACS merges storm track data from agencies all around 202  
the world and as such it requires careful processing, particularly for wind and 203  
sea-level pressure data. Here, we use the same IBTrACS version (v04) and 204  
post-processing procedure for IBTrACS data as in Bourdin et al (2022). In 205  
particular: 206  
207

- we retrieve surface wind and sea-level pressure data by prioritizing, for each 215  
basin, data provided by the WMO agency responsible for that location. For 216  
WMO values coming from a U.S agency, we convert them to 10-minute winds 217  
using a 1.12 correction factor. If the responsible WMO agency is lacking 218  
wind data, we attempt the following: 219  
220  
221  
222
  - we average the data available among the following centers: Tokyo, 223  
Réunion, BoM, Nadi and Wellington; 224  
225
  - if still missing, we use the wind data from USA agencies using a 1.12 226  
correction factor to convert them from 1-minute to 10-minutes winds; 227  
228  
229  
230

6 *Assessing the representation of tropical cyclones in ERA5 with the CNRM tracker*

231 – if still missing, we use values from the Chinese Meteorological Adminis-  
232 tration (CMA) values using a 1.08 correction factor to convert values to  
233 10-minutes winds;  
234

235 – The remaining missing values are classified as such.  
236

237 • we remove tracks referenced as 'spurs' in the metadata;  
238

239 • we only keep 6-hourly data (rather than 3-hourly) and remove tracks shorter  
240 than 24 hours;  
241

242 • we only retain cyclonic seasons from 1981 to 2019 in both the northern and  
243 southern hemispheres (39 seasons).  
244  
245

246 Recovering missing SLP values is done similarly as for wind data, except no  
247 conversion is needed and therefore we average the available data from Tokyo,  
248 Réunion, BoM, Nadi, Wellington, USA and CMA.  
249  
250  
251

## 252 **2.2 Tracking Scheme**

253 We use the CNRM Tropical Cyclone Tracking Scheme (Chauvin et al, 2006)  
254 to detect and track tropical cyclones in the ERA5 reanalysis. The tracking is  
255 done separately for each hemisphere up to 60° latitude and operates in three  
256 steps which are described below.  
257  
258  
259  
260  
261

### 262 **Detection**

263 Detection of candidate points is first based on a relative 850 hPa vorticity  
264 threshold (**VOR**). A local sea-level pressure minimum is then sought within a  
265  $10^\circ \times 10^\circ$  box around the candidate which is then considered to be the system's  
266 center.  
267  
268  
269  
270

271 We then compute the characteristic size of the system based on either the  
272 sea-level pressure gradient maxima or the radius of maximal tangential wind  
273 — whichever one is the smallest — which we call the *Reference Disk Radius*  
274  
275  
276



(RDR). This allows us to separate the presumed cyclone from its environment, which is defined as a disk with a radius of three times the RDR, delimiting a surface that is nine times larger than the TC itself. Separating the presumed TC from its environment allows to check for temperature anomaly which is calculated as the difference between the temperature inside the circle delimited by the RDR and the temperature inside the environment (RDR excluded). More specifically, the detection process tests for the following:

- Temperature anomaly: The sum of temperature anomalies at 700, 500 and 300 hPa is to be greater than a threshold hereafter noted **TANOM**;
- Surface wind speed: the 10 meter maximum surface wind speed within the RDR is to be greater than a threshold hereafter noted **RES**;
- Warm upper core: the 300-850 hPa temperature anomaly gradient is to be greater than a threshold hereafter noted **PT**. This criterion defines to what extent the core should be warmer in the upper levels than in lower levels;
- Stronger wind in lower levels: the 300-850 hPa mean wind speed gradient within the RDR is to be greater than a threshold hereafter noted **PW**. This criterion defines to what extent the wind speed in upper levels should be weaker than that in lower levels, as a result of the thermal wind balance applied to the warm core.

For the present study, we used  $\mathbf{VOR} = 15 \cdot 10^{-5} \text{ s}^{-1}$ ;  $\mathbf{TANOM} = 1 \text{ K}$ ;  $\mathbf{RES} = 5 \text{ m.s}^{-1}$ ;  $\mathbf{PT} = -1 \text{ K}$  and  $\mathbf{PW} = 5 \text{ m.s}^{-1}$ . These values were selected based on the results of the sensitivity study presented in Appendix A

## Linking

Linking points together is the process of joining the individual points resulting from the detection process into tracks. In the CNRM TC Tracking Scheme, this is achieved by an iterative process that selects the candidates that maximize

323 the smoothness of the overall trajectory. Originally based on the methodology  
324 from Hodges (1994), our tracking scheme maximizes smoothness by combining  
325 three quality parameters that each minimize a distance measurement while  
326 also factoring the maximum distance a TC is capable of covering in a single  
327 time step.  
328  
329

330  
331 Knowing the position at time  $t$ , we select the next position from the can-  
332 didates at time  $t + 1$  as follows: The first parameter measures the euclidean  
333 distance between the position at time  $t$  and the candidate at  $t + 1$ . The sec-  
334 ond parameter measures the euclidean distance from the forward extrapolated  
335 position from the track at  $t - 1$  to the candidate at  $t + 1$ . Finally, the third  
336 parameter measures the distance from the backward extrapolated position  
337 from the track at  $t + 2$  to the position at time  $t$ . By iteratively evaluating the  
338 total quality index for each candidate and at each time step, we ensure that  
339 the resulting track shows the least possible amount of inconsistencies, such as  
340 sharp turns and fragmented patterns.  
341  
342  
343  
344  
345  
346  
347  
348

### 349 **Relaxation**

350  
351 In order to avoid the issue where a single TC track might be split into several  
352 parts due to one of the parameter falling below its threshold – thereby leading  
353 to an incorrect TC count – the tracking scheme performs what is called the  
354 relaxation process.  
355  
356

357  
358 During relaxation, all detection thresholds are lifted and the tracking  
359 scheme completes tracks both forward and backward by searching for a vortic-  
360 ity maxima within a 500 km radius disk centered around the advected position  
361 of the system computed from the two previous time steps. This process goes  
362 on in both directions until the vorticity maxima falls below a newly defined  
363 threshold, referred to as the relaxation level. Because several detected tracks  
364 can – prior to the relaxation process – belong to the same TC, relaxing all  
365  
366  
367  
368

detected tracks can result in overlapping duplicate trajectories. For that reason, a final step in which such duplicates are identified and removed is applied. This is done by eliminating relaxed tracks that have more than five steps in common with an already existing track. Throughout this study, the relaxation level is set at  $25 \cdot 10^{-5} s^{-1}$ . While the relaxation level is also a tunable threshold, it does not affect the number of detected TCs like the parameters described in 2.2 do but rather the length of the detected tracks.

### Post-processing

Post-processing techniques can be used to retrospectively filter out extratropical cyclones and other mid-latitude lows that might have passed the detection tests. In this study, we use the thermal wind warm core diagnosis developed in Hart (2003) and tested in Bourdin et al (2022), hereafter referred to as the VTU. This method uses the  $V_U^T$  parameter from Hart's phase space — defined as the vertical derivative of the isobaric height perturbation within the 600–300 hPa tropospheric layer — to diagnose the presence of a warm upper core. Using the implementation from Bourdin et al (2022), the  $V_U^T$  parameter is computed as follow:

$$V_U^T = P_{\text{mid}} \frac{\Delta Z|_{600 \text{ hPa}} - \Delta Z|_{300 \text{ hPa}}}{\Delta P}$$

where  $\Delta Z|_p$  is the maximum isobaric height perturbation within a 500 km radius at the pressure level  $p$ , and  $P_{\text{mid}} = (600 + 300)/2 = 450$  hPa. The  $V_U^T$  parameter is computed for each point of the relaxed tracks. A given track is removed from the dataset if it presents less than six time steps where  $V_U^T$  is strictly positive, or if not all time steps verify  $V_U^T > 0$  for tracks that last less than 36 hours. We stress that the VTU post-processing is not used in the sensitivity study presented in Appendix A.

## 415 **2.3 Track pairing method**

416

417 We use a track pairing algorithm to pair detected tracks from ERA5 with those  
418 from the IBTrACS observational dataset. This allows us not only to provide  
419 detailed analysis of the performances of our tracking scheme over ERA5, but  
420 it also allows us to better evaluate TCs representation in the reanalysis as  
421 we can focus on tropical cyclones that have been successfully matched with  
422 IBTrACS, thereby eliminating possible biases that could come from spurious  
423 detections, i.e systems incorrectly classified as tropical cyclones.

428

429 The track pairing algorithm works by searching for tracks in IBTrACS that  
430 match both spatially and temporally to the detected systems in the reanalysis.  
431 More specifically, the algorithm starts by assigning each detected track a geo-  
432 graphic basin. Figure B3 from the appendix presents the basins boundaries,  
433 which are adapted from Knutson et al (2020) so that the separation between  
434 the Easter Pacific basin (EPac) and the North Atlantic basin (NAtl) follows  
435 the American coast. For each detected track in a given basin, we start by  
436 searching for potential matches in IBTrACS by selecting tracks that have at  
437 least one time stamp in common (temporal overlapping). Then for each candi-  
438 date track, we compute the great-circle distances between the detected track's  
439 positions and the candidate's at equal time stamps. A detected position is  
440 considered to be found in IBTrACS if the great-circle distance between ERA5  
441 and IBTrACS for that time step is less than 300 km. Thus for each IBTrACS  
442 candidate we compute the coverage ratio defined as the amount of detected  
443 time steps located less than 300 km from the candidate divided by the candi-  
444 date's length. The candidate with the highest coverage ratio is selected and the  
445 detected track is considered successfully paired with a track from IBTrACS.

456

457 Note that in these conditions, a single time step satisfying the distance  
458 threshold can be enough to consider that the entirety of the ERA5 track is

460

indeed found in IBTrACS. However, as it is highly improbable that two TC systems evolve at the same time at less than 300 km from each other, we assume that if a 'match' is found for one time step, then it should correspond to the same TC. This process produces basin specific data that may then be aggregated with other regions to produce pseudo-global information. We point out that we systematically exclude the North Indian region from our analyses due to reliability issues within IBTrACS in this region, as well as the South Atlantic basin due to the general lack of cyclonic activity.

With the resulting data, we can evaluate the performance of the tracking scheme by computing both the Probability of Detection (POD) and the False Alarm Rate (FAR), defined as follow:

$$\text{POD} = \frac{N_{\text{Hit}}}{N_{\text{IBTrACS}}} \quad \text{FAR} = \frac{N_{\text{ERA5}} - N_{\text{Hit}}}{N_{\text{ERA5}}}$$

Where  $N_{\text{IBTrACS}}$  is the number of reported tracks in IBTrACS,  $N_{\text{ERA5}}$  is the number of detected tracks in ERA5 and  $N_{\text{Hit}}$  is the number of detected tracks that are paired with IBTrACS.

## 3 Results

### 3.1 Detection score

In this section we focus on characterizing the performances of our TC tracking scheme applied to ERA5 over the 1981 to 2019 cyclonic season range. The tracking scheme was run with the detection thresholds from Section 2.2, which were obtained from the tuning experiment described in Appendix A and was done for each hemisphere separately from 0° to 60°. The VTU method from Section 2.2 was also used to remove extra-tropical tracks and hence further reduce the FAR. Figure 1 presents the integrated FAR and POD over the 1981

507 - 2019 period while Table 1 summarizes the yearly FAR and POD time series  
508 over this period.  
509

510

511

512

513

514

515

516

517

518

519

520

521

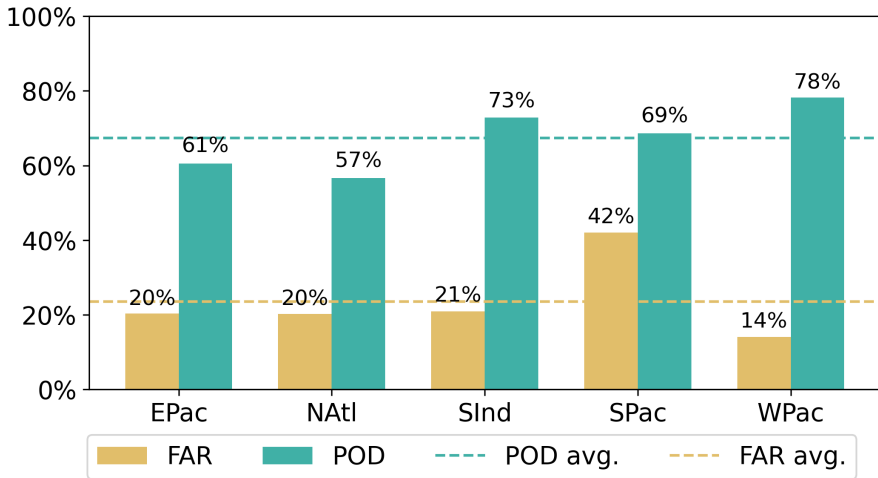
522

523

524

525

526



527 **Fig. 1** FAR and POD over the 1981 - 2019 seasons for all five basins of interest. Dotted  
528 lines represent the averages over these regions.

529

530

531

532

533

534

535

536

537

538

539

540

541

542

543

544

545

546

547

548

549

550

551

552

The probability of detection shows disparities between regions. The SInd and WPac both outperform all three other basins with respectively 73 % and 78 %. The NATl basin on the other hand has the lowest POD of all five with only 57 %, followed by the EPac at 61 %. The NATl basin is the region showing the highest decrease in POD due to the VTU filter: All other regions show a POD decrease ranging from 1 to 2 points after applying the filter, but the NATl basin however drops from 68 % to 57 %, i.e 11 points (accounting for 71 tracks). This could be explained by the fact that the NATl region in IBTrACS has the most septentrional data records of all basins. Indeed, as the latitude increases, the amount of records where IBTrACS reports a Nature of either 'Not Reported' or 'Extra Tropical' increases, and systems in IBTrACS that correspond to the tracks that are removed from ERA5 through the VTU filter are found to evolve in higher latitudes than the ones missed the same way

in the other regions (Figure B4 in Appendix B). It seems therefore possible that the VTU filter removed tracks that might have lost their tropical nature in IBTrACS and didn't present a strong enough upper tropospheric thermal wind in ERA5 to be kept in the dataset.

In contrast, the FAR is fairly consistent between basins except for the SPac which presents the highest FAR with 42 % while the WPac shows the lowest FAR with 14 %, in addition to having the best POD. Averaging over the five regions, we get a 67 % POD and 24 % FAR. The slight difference in globally averaged FAR we note compared to what Bourdin et al (2022) found when using the VTU filter on the CNRM Tracking Scheme can probably be explained in large part by the differences in how the VTU post-processing is applied, and also to the fact that we do not include here the North Indian region in the analysis.

However, these integrated values hide large inter-annual variations as shown by Table 1. Most notably, the SPac basin experiences the strongest variations in both the FAR and POD with a standard deviation of 18.7 % and 21.2 % respectively and also has the highest 95<sup>th</sup> FAR percentile with 66.6 %. Along with the SInd basin, the SPac also presents a 95<sup>th</sup> POD percentile of 100 %. Conversely, WPac is the most consistent basin with a standard deviation below 10 % for both metrics, the lowest 95<sup>th</sup> FAR percentile and highest 5<sup>th</sup> POD percentile.

Figure 2 presents the probability density map for a detected track for both a successfully matched track and one flagged as false alarm, after application of the VTU filter. In the EPac and the SInd basins, the region of activity are the same for both groups of tracks. On the other hand in the WPac, SPac and the NATl basins, false alarms are seen to evolve predominantly at higher latitudes. False alarms tracks are usually shorter lived and marginally

**Table 1** Statistical summary of yearly FAR and POD timeseries from 1981 to 2019

Basin	FAR (%)				POD (%)			
	5 %	95 %	mean	std	5 %	95 %	mean	std
<b>EPac</b>	0.0	38.6	20.4	11.3	30.1	89.1	62.2	17.3
<b>NAtl</b>	0.0	43.6	21.4	16.2	28.2	79.1	54.7	16.1
<b>SInd</b>	0.0	44.7	18.7	12.8	46.3	100.0	74.5	18.6
<b>SPac</b>	17.5	66.6	43.9	18.7	34.9	100.0	67.8	21.2
<b>WPac</b>	3.1	27.4	14.1	7.6	64.3	93.1	78.5	9.9
<b>Global</b>	15.4	29.1	21.8	4.6	53.5	79.2	69.2	8.5

weaker than their counterparts but still pass the detection tests, making it difficult to filter them out dynamically during the tracking process. This is especially true given the results from A, as increasing detection thresholds has the side-effect of strongly penalizing the POD. While some amount of tropical false alarms is likely unavoidable when comparing the output of an objective tracking scheme with a reference dataset that has an inherent part of subjectivity, the false alarm density probability above 45° in Figure 2 shows that the VTU post-processing fails to remove all mid-latitudes systems. This can be explained by considering two factors: On one hand, the  $V_U^T$  parameter is estimated here using only two pressure level within the considered tropospheric layer. It is therefore possible that computing the parameter by fitting the vertical profile of  $\Delta Z$  to the log of the pressure levels within the layer instead — as suggested by Hart (2003) — would yield a more accurate estimation of the parameter's sign. Secondly, because the VTU method negatively affects the POD in a non-negligible way, the filtering rule needs to express a balance between its efficiency in removing false alarms and the cost in POD. Increasing the required amount of time steps where  $V_U^T > 0$  holds ultimately reaches a point of diminishing returns where the loss in POD is too great compared to the improvement in filtering efficiency.



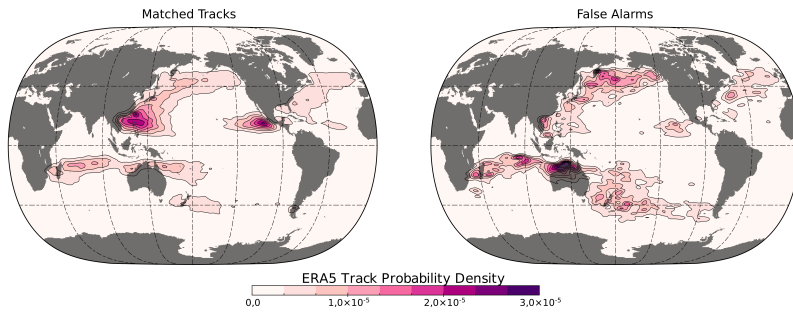


**Fig. 2** Probability density map of passage of an ERA5 track for (left) one that is matched to IBTrACS and (right) one that is flagged as false alarm. Computed through kernel density estimation with an anisotropic Gaussian kernel with respectively  $3^\circ$  and  $1^\circ$  zonal and meridional standard deviation over a  $0.25^\circ$  resolution spatial grid.

### 3.2 TC intensity

We focus in this section on how TCs are represented physically and dynamically in ERA5. For this purpose, we filter out detected tracks flagged as false alarms to only keep the ones successfully matched to IBTrACS. Figure 3 represents the wind-pressure relationship (WPR) for the set composed of all temporally and spatially matching points in each track pair, as described in 2.3. Using a  $V = a\Delta P^b$  relationship (Atkinson and Holliday, 1977) to fit on both groups of points, we get  $a = 3.15$  and  $b = 0.54$  for ERA5 and  $a = 1.4$  and  $b = 0.8$  for IBTrACS. Both relationships are therefore vastly different with a faster falling SLP curve in ERA5 compared to IBTrACS. As a result, the wind speeds in ERA5 are considerably lower than in IBTrACS with a 95<sup>th</sup> percentile of  $28.5 \text{ m}\cdot\text{s}^{-1}$  for the reanalysis – which corresponds to a tropical storm on the Saffir-Simpson Hurricane Wind Scale (SSHWS) – compared to  $50.5 \text{ m}\cdot\text{s}^{-1}$  for the observational records.

However, the marginal densities on Figure 3 show that the SLP distribution in ERA5 is better represented than the wind speed and can reach reach category 4 on the revised SSHPS from Klotzbach et al (2020) (99.8<sup>th</sup> percentile) and even reaches category 5 with an absolute minimum of 923 hPa. This difference in how well both variables are represented results in a WPR that is

645  
646  
647  
648  
649  
650  
651  
652  
653  
654

655  
656  
657  
658  
659  
660  
661  
662  
663  
664  
665  
666  
667  
668  
669  
670  
671  
672  
673  
674  
675  
676  
677  
678  
679  
680  
681  
682  
683  
684  
685  
686  
687  
688  
689  
690

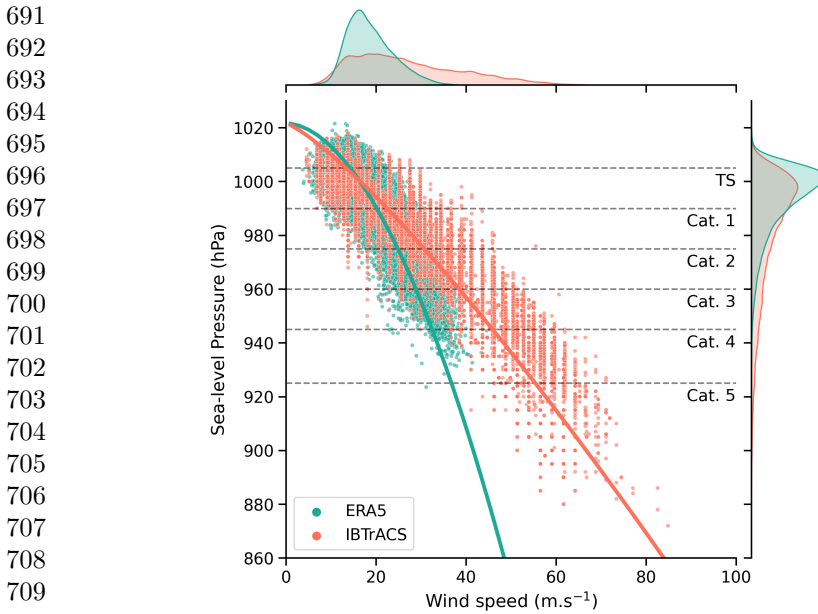


**Fig. 3** Pressure-Wind relationship from the subset of matching points in all paired tracks. 58,920 data points in each group. Solid lines show the  $V = a\Delta P^b$  fits and the reference SLP at the intercept is set to be greater than the highest SLP record. The marginals represent the density distributions of the data projected on each axis. Horizontal dotted lines represent the pressure-based Saffir-Simpson Hurricane Scale (SSHS) intensity class thresholds from [Klotzbach et al \(2020\)](#)

less consistent with IBTrACS and also with ERA-I. Indeed [Murakami \(2014\)](#) compares the WPR diagrams in the northern hemisphere for IBTrACS and six reanalysis products including ERA-I, and finds that the maximum wind speed in ERA5 predecessor extends up to a little more than  $30 \text{ m.s}^{-1}$  (which is only marginally weaker than what we find in ERA5) but also that the minimum SLPs are much less deep, as ERA-I struggles to go below 960 hPa. This comparatively better WPR in ERA-I (despite having weaker TCs) is also found in [Hodges et al \(2017\)](#).

Figure 4 then illustrates the relationship between ERA5 and IBTrACS SSHPS intensity classes by classifying TCs from paired tracks over their entire life cycle. A general agreement between the intensity classes of both datasets is apparent with the majority of entries located below the main diagonal, which is

expected as model’s horizontal resolutions prevent the accurate representation of TC intensity (Davis, 2018). However, the spread in the reanalyzed SSHPS classes — representative of the uncertainty associated to the TC intensity in ERA5 — increases with the intensity of the TCs in IBTrACS. For instance, 31 Cat 5 TCs in IBTrACS are reanalyzed into systems rated below Cat 1, amounting to 11.4 % of the total number of Cat 5 IBTrACS TCs represented here.

ERA5	Cat 5	0	0	0	0	0	1	1
	Cat 4	0	0	3	0	6	7	21
	Cat 3	0	1	5	11	30	67	76
	Cat 2	0	3	15	69	89	105	81
	Cat 1	0	16	182	152	131	102	62
	TS	0	269	324	131	119	91	28
	TD	4	43	12	9	2	0	3
		TD	TS	Cat 1	Cat 2	Cat 3	Cat 4	Cat 5
		IBTrACS						

**Fig. 4** Confusion matrix between ERA5 and IBTrACS SSHS intensity classes over the five basins of interest. TCs are categorized using the pressure-based SSHS intensity thresholds from Klotzbach et al (2020).

The opposite effect also occurs but is much rarer. The confusion matrix is indeed non-triangular and shows 3 % of track pairs as being more intense in ERA5 than in IBTrACS. This effect is the most notable for IBTrACS Tropical Storm (TS) category for which this number reaches 6.4 % and with one system in ERA5 that reaches Cat 3. Finally, while the relative agreement between maximum intensities from Figure 4 holds when considering the global scale, results can vary for different basins as seen on Figure B5 from the appendix. Most notably, the confusion matrix for the NAatl region is the most diagonal

783 and shows very little spread while EPac on the contrary presents very little  
784 consistency with most systems in ERA5 being classified as TS, independently  
785 of the observed intensity.  
786  
787

788

### 789 **3.3 Life cycle**

790

791 Figure 5 compares the average lifecycle between matched TCs from ERA5 and  
792 IBTrACS, centered around the maximum wind speed at day 0. The sample  
793 sizes (top panels) are of different shape around the center due to ERA5 tracks  
794 not necessarily having the same length as their IBTrACS match, thus indicat-  
795 ing that detected tracks in the reanalysis tend to be shorter than in IBTrACS.  
796 As also shown by Figure 3, Figure 5 highlights the low wind intensity in ERA5  
797 with a mean maximum wind speed at day 0 of  $23.2 \text{ m.s}^{-1}$  against  $38.1 \text{ m.s}^{-1}$   
798 in IBTrACS. Furthermore, the relative standard deviation — defined as the  
799 ratio of the standard deviation over the sample mean at each time step — is in  
800 fact smaller for ERA5 as it ranges from 24 % to 31 % against 34 % to 50 % for  
801 IBTrACS, with day 0 having the lowest relative standard deviation for both  
802 datasets.  
803  
804

805 The shapes of both life cycles are distinguished by a few key differences which  
806 are better shown in the bottom panels of Figure 5, representing the change  
807 rate of the mean wind speed. The life cycle in ERA5 is almost linear outside of  
808 the  $[-2; +2]$  day range, with the intensification phase having a slightly steeper  
809 slope than during the weakening phase and also exhibits a sharp spike around  
810 day 0 with great symmetry. In IBTrACS however, the intensification phase is  
811 curvilinear with an almost linearly increasing change rate before day  $-2$ . The  
812 peak around day 0 is not symmetric with the left side showing a sharp inten-  
813 sification until the maximum, followed by a slower decrease and the tipping  
814 point occurs slightly later than day 0. This dissymmetry comes solely from the  
815  
816  
817  
818  
819  
820  
821  
822  
823  
824  
825  
826  
827  
828

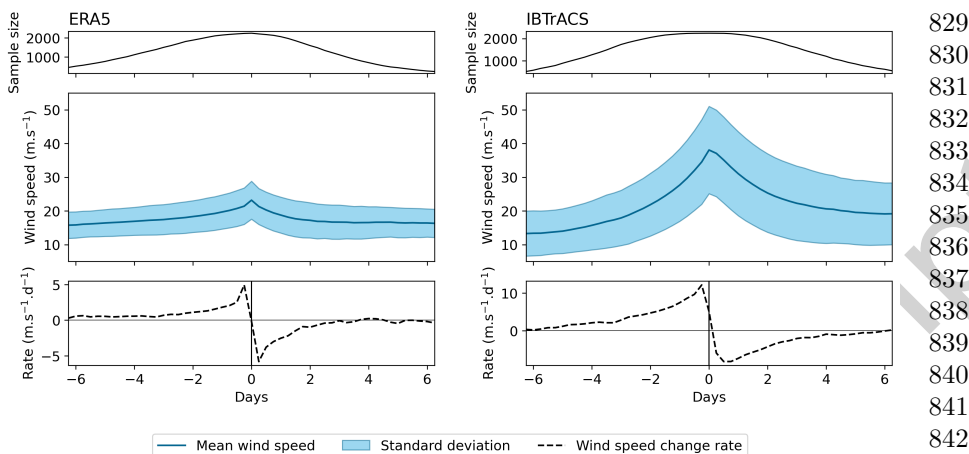


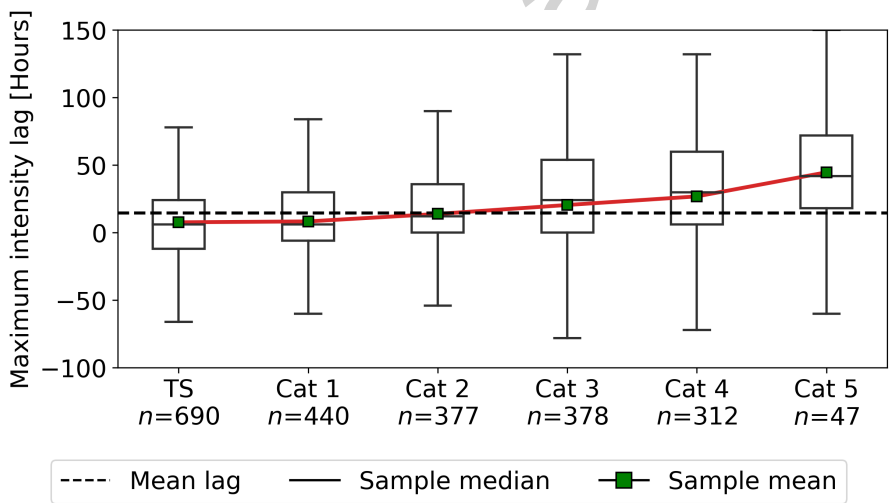
**Fig. 5** Mean TC life cycles in (left) ERA5 and right (IBTrACS) from the set of matching tracks. Life cycles are centered around the time of maximum wind speed and integrated over the five basins of interest. Both upper panels show for each time step the size of the sample used to compute the mean and standard deviation. Lower panels present the derivative of the mean wind speed. The X axis goes from -6.25 to +6.25 days with 0 being the maximum intensity. The Y axes on the bottom row plots are not aligned.

method used to identify the time step of the maximum wind speed; here we select the first occurrence in cases where the maximum wind speed is found on consecutive time steps. Using the last occurrence would yield a mirrored effect, while selecting the central occurrence would even it out. But this subtlety nevertheless illustrates one of the main difference between TCs from the reanalysis and those from the observations, in that TCs in ERA5 appear to be unable to plateau at their maximum intensity like they do in IBTrACS.

Figure 6 represents the distributions of the delays between life cycle from each pair of tracks and for each SSHWS class. A positive lag between two life cycles indicates that the reanalyzed TC reached its maximum intensity later than in IBTrACS. The mean delay across all categories is of 13.3 hours, i.e slightly greater than two time steps (significantly different from 0). Distributions for each class appear to shift towards higher values with TS presenting a 7.7 hours average lag. Starting with Cat 2, the mean lag reaches the overall average and extends to 44.7 hours for Cat 5. All intensity groups have a mean

829  
830  
831  
832  
833  
834  
835  
836  
837  
838  
839  
840  
841  
842  
843  
844  
845  
846  
847  
848  
849  
850  
851  
852  
853  
854  
855  
856  
857  
858  
859  
860  
861  
862  
863  
864  
865  
866  
867  
868  
869  
870  
871  
872  
873  
874

875 statistically significantly different from 0 under a 5 % confidence level two-  
 876 sided student test. This shift towards higher delays in maximum intensities  
 877 between ERA5 and IBTrACS could be explained by the lack of rapid intensifi-  
 878 cation in the reanalysis. It should be noted that in cases where the maximum  
 879 wind speed occurs on several consecutive time steps in IBTrACS — and con-  
 880 trary to the method used for Figure 5 — we select the central occurrence (or  
 881 the one before if the plateau extends over an even number of time steps) so  
 882 that we measure the lag with respect to the middle of the maximum intensity  
 883 plateau. This is done in order to improve the interpretability of these results.  
 884 The choice of the occurrence to use in such cases acts in fact as an offset to all  
 885 distributions but has virtually no impact on the placement of each box plot  
 886 relative to each other and to the overall mean.  
 887  
 888  
 889  
 890  
 891  
 892  
 893  
 894



911 **Fig. 6** Distributions of the maximum intensity delays between paired tracks for each SSHS  
 912 category. Categories are based on IBTrACS maximum wind speed. The delay is relative to  
 913 IBTrACS such that a positive lag indicates a later intensity peak in ERA5.  
 914

915  
 916  
 917  
 918  
 919  
 920

### 3.4 Internal structure

Lastly, figures 7 and 8 show the composite azimuthally averaged cross-section of detected TCs in the reanalysis for both the radial and tangential wind as well as the temperature anomaly and for each SSHS intensity class. These composites are aggregated based only on the intensity of the observed track (i.e. IBTrACS) for matched tracks, independently of how intense the TC is in the reanalysis at those times. The amount of averaged time steps for each SSHS category are presented in Table 2. With this methodology, these composite figures therefore show us the average ERA5 representation of an observed TC from a given SSHS category.

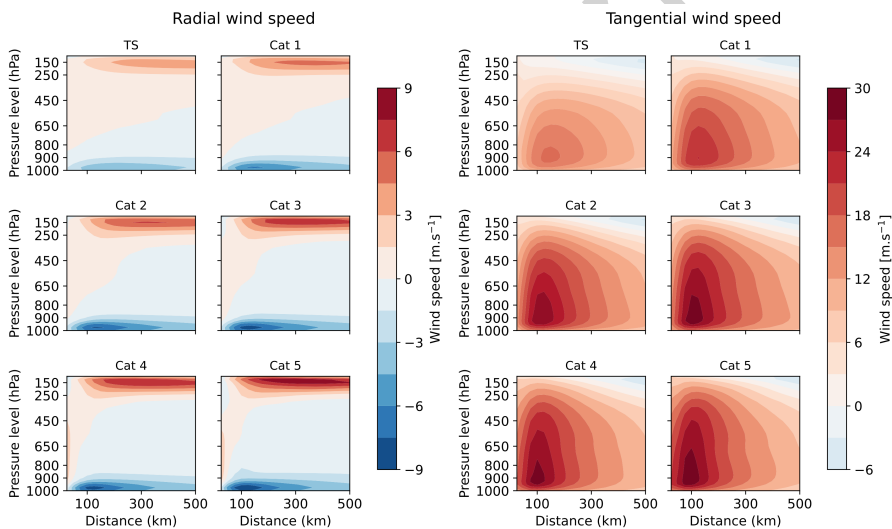


**Fig. 7** Radius-height composites cross-sections of azimuthally averaged radial (left) and tangential (right) wind speed of detected TCs in ERA5 sorted by IBTrACS SSHWS categories. Each panel is made from the set of matching time steps where the observed track is at the given SSHWS intensity. The azimuthal mean is computed within a  $41 \times 41$  point horizontal box and 27 vertical levels ranging from 1000 to 100 hPa.

The radial wind is seen to move towards the center near the surface, from 1000 hPa up to 900 hPa and then flows outwards radially in the upper part of the atmosphere from 200 hPa up to 100 hPa which demonstrates the low level

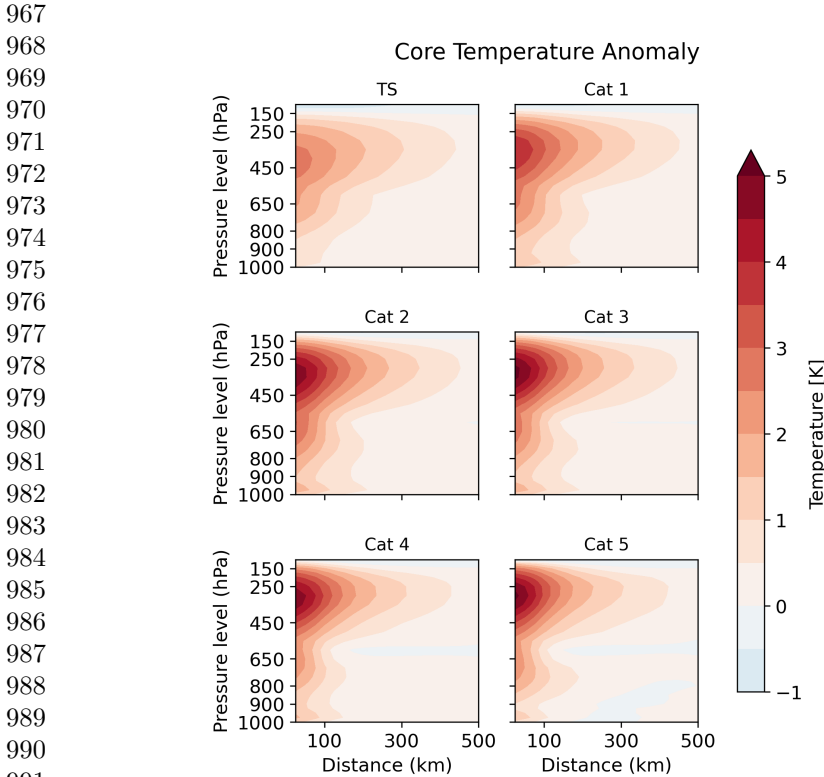


**Fig. 8** As in Figure 7 but for the temperature anomaly. The reference temperature is computed from the four corners of the  $41 \times 41$  box, i.e from points 500 to 700 km away from the center.

**Table 2** The amount of time steps that are averaged to produce the radius-height composites from Figures 7 and 8, for each SSHS category. Below are presented general characteristics for the tangential wind speed and core temperature anomaly for all intensity categories.

	TS	Cat 1	Cat 2	Cat 3	Cat 4	Cat 5
Count	27,047	10,065	6,514	3,953	1,894	205
	<b>Tangential Wind Speed</b>					
Maximum wind speed (m/s)	16.5	22.6	27	28.7	28.6	29.7
Height of max. wind speed (hPa)	900	900	900	925	925	925
Radius of max. wind speed (km)	150	125	125	100	100	100
	<b>Core Temperature Anomaly</b>					
Maximum anomaly (K)	2.74	3.99	4.89	5.14	4.87	5.16
Height of max. anomaly (hPa)	400	350	350	300	300	300
Radial gradient (K per 100 km)	-0.69	-1.22	-1.73	-1.89	-1.88	-2.31



convergence and the upper-level divergence. Radial wind speed varies from 1013  
−4.3 to 3.9 m.s<sup>−1</sup> for the TS group and increases up to 9 m.s<sup>−1</sup> for Cat 5 in 1014  
both directions. The tangential wind speed profile tightens around the core as 1015  
intensity increases. The maximum wind speed is located at the 900 hPa level 1016  
and 150 km from the center for TS, within the 15 – 18 m.s<sup>−1</sup> range, and is 1017  
located at 925 hPa and 100 km from Cat 3 to 5, for which it reaches the 27 – 1018  
30 m.s<sup>−1</sup> bin with a maximum of 28.9 m.s<sup>−1</sup>. The temperature anomaly from 1019  
Figure 8 exhibits the same tightening around the core as for the tangential 1020  
wind. This tightening can be quantified in terms of mean radial temperature 1021  
gradient taken at the pressure level of maximum anomaly and computed until 1022  
the anomaly decreases by 50 %, thus representing the temperature anomaly 1023  
decrease rate close to the core. The mean radial temperature gradient decreases 1024  
with SSHS categories from −0.69 K per 100 km for TS down to −2.31 K per 1025  
100 km for Cat 5. Values for the remaining SSHS categories are presented in 1026  
Table 2. Maximum temperature anomalies range from 2.74 K for the TS group 1027  
up to 5.16 K for Cat 5. The maximum temperature anomaly increases for each 1028  
SSHWS category except for Cat 4 where it drops from 5.14 K (Cat 3) to 4.87 K 1029  
(Cat 4). A similar decrease in intensity from Cat 3 to Cat 4 is also noted for the 1030  
tangential wind speed (Table 2). The fact that this decrease can be seen in both 1031  
variables is expected because the warm core from a TC is linked to its primary 1032  
circulation through the gradient and thermal wind balance (Willoughby, 1990). 1033  
It is however interesting to note that the temperature radial gradient does not 1034  
follow the same pattern as it either increases or remains constant throughout 1035  
all SSHS categories. Lastly, the height of the maximum temperature anomaly, 1036  
defined as the level at which maximum temperature anomaly at 25 km from 1037  
the center is reached, also increases with intensity. The maximum temperature 1038  
anomaly is located at 400 hPa for TS, 350 hPa for Cat 1 and 2 and 300 hPa 1039  
for Cat 3 to 5. 1040  
1041  
1042  
1043  
1044  
1045  
1046  
1047  
1048  
1049  
1050  
1051  
1052  
1053  
1054  
1055  
1056  
1057  
1058

1059 The smooth intensity increase with SSHS categories depicted here is how-  
1060 ever to be nuanced by the fact that these composites are the result of strong  
1061 averaging — first azimuthally and then over many time steps and different sys-  
1062 tems — which tends to smooth out imperfections. Figure B6 from the appendix  
1063 present the distributions of the maximum tangential wind speed and maximum  
1064 temperature anomaly for each radius-height cross-section and for each SSHS  
1065 category and show a large intensity spread in each class, as also pointed out  
1066 by Figure 4. For instance, the 5<sup>th</sup> percentile for the Cat 5 maximum tangen-  
1067 tiel wind speed is  $19.6 \text{ m.s}^{-1}$ , which is halfway between the mean maximum  
1068 wind speeds from the TS and Cat 1 categories. Conversely, the TS category  
1069 exhibits a 95 % percentile of  $30.8 \text{ m.s}^{-1}$ , which is stronger than the mean Cat  
1070 5 maximum wind speed from Table 2.  
1071  
1072  
1073  
1074  
1075  
1076  
1077  
1078

1079 Overall, the visual differences in internal structure for all composite vari-  
1080 ables from Figures 7 and 8 are the strongest from Cat 1 to 3. This includes both  
1081 the tightening of the wind vortex with SSHWS category, the tightening and  
1082 elevation of the warm core and also the strengthening of the radial fluxes from  
1083 the radial wind composites. Above Cat 3, TCs' internal structures produced  
1084 by ERA5 become almost indistinguishable, as also highlighted in Table 2. This  
1085 inability to distinguish TCs above Cat 3 is consistent with ERA5 underesti-  
1086 mation of TC intensity in general, as seen from Figures 3, 4 and 5. Combined  
1087 with the aforementioned uncertainty in the intensity of reanalyzed TCs, this  
1088 effect could likely explain the apparent drop in intensity between Cat 3 and  
1089 Cat 4.  
1090  
1091  
1092  
1093  
1094  
1095  
1096  
1097  
1098

## 1099 4 Discussion and Conclusion

1100  
1101 As a preliminary part of our work, we conducted a sensitivity analysis of the  
1102 CNRM TC Tracking Scheme to its five different detection thresholds with  
1103  
1104

respect to the FAR and POD metrics, which is described in Appendix A. 1105  
The ultimate purpose of the analysis was to use this information to make 1106  
an informed choice of threshold values for the complete ERA5 tracking, such 1107  
that both detection metrics would be optimized to some extent. The analysis 1108  
provided interesting insights about the tracking scheme with the maximum 1109  
surface wind and core temperature anomaly thresholds (**RES** and **TANOM**) 1110  
having the biggest influence on the tracker's performance. Most strikingly, it 1111  
showed that lowering **RES** to 10 and 5 m.s<sup>-1</sup> consistently improved FAR and 1112  
POD compared to RES=15. This is irregular since most tracking schemes tend 1113  
to use wind speed thresholds of at least 15 m.s<sup>-1</sup> (Walsh et al, 2007; Ullrich 1114  
and Zarzycki, 2017, Appendix B). But this is not to say that a 5 m.s<sup>-1</sup> wind 1115  
speed is considered cyclonic in ERA5. In fact, the **RES** threshold only has 1116  
a limited impact on the wind speed distribution from the final set of tracks. 1117  
Indeed, while 10 m.s<sup>-1</sup> can be seen as a more physically acceptable value for 1118  
the surface wind speed threshold when considering the underestimation of TC 1119  
intensity in ERA5, it must be noted that the wind speed distributions from 1120  
the RES=5 and RES=10 non-paired set of tracks in the NATl basin — all 1121  
other thresholds held constant — are almost identical (not shown), which is 1122  
consistent with the observed POD saturation on Figure A1 at RES=10. The 1123  
mean wind speeds from these two distributions are non-significantly separated 1124  
by 0.1 m.s<sup>-1</sup> (p-value = 0.2). The amount of values strictly below 10 m.s<sup>-1</sup> are 1125  
5.3 % and 4.9 % for RES=5 and RES=10, respectively. For RES=15, the mean 1126  
wind speed is only 1 m.s<sup>-1</sup> greater than that of RES=10. The reason for the 1127  
low impact of the **RES** parameter on the measured wind speed distribution is 1128  
twofold. First, during the detection process, all detection criteria must be held 1129  
for at least 4 time steps for the track to be kept, meaning that any track not 1130  
maintaining a maximum wind speed greater than **RES** for at least 24 hours 1131  
1132  
1133  
1134  
1135  
1136  
1137  
1138  
1139  
1140  
1141  
1142  
1143  
1144  
1145  
1146  
1147  
1148  
1149  
1150

1151 will be discarded. The second reason is that the relaxation process completes  
1152 tracks forward and backward with no other requirement than a set relative  
1153 vorticity threshold and is intended to capture the genesis and ending of TCs,  
1154 where wind speeds are the weakest. This particular aspect results in the lower  
1155 end of the wind speed distributions to remain about the same, independently  
1156 of the **RES** parameter. Lowering this threshold therefore mostly affects the  
1157 number of detected tracks, which is why it acts as a POD upper bound.  
1158

1162 The performances of the tracking scheme on ERA5 from 1981 to 2019 —  
1163 presented in Section 3.1 — show FAR and POD that vary from basin to basin,  
1164 with a 67 % mean POD and 24 % mean FAR. Bourdin et al (2022) conducted  
1165 an inter-comparison analysis of four tracking schemes on ERA5, including our  
1166 own, for which we provided a set of tracks produced with the same parameters  
1167 than here and uses a post-processed sub-tropical jet (STJ) diagnostic as cut-off  
1168 latitude to filter out mid-latitude systems, which is applied over all four track-  
1169 ing schemes. This study places the CNRM TC Tracking Scheme’s probability  
1170 of detection on par with the OWZ (Tory et al, 2013) and UZ (Ullrich et al,  
1171 2021) tracking schemes, both in terms of globally averaged POD and inter-  
1172 regional differences. However, without any form of mid-latitude filtering, both  
1173 these tracking schemes present considerably less false alarms than the CNRM  
1174 scheme. Moreover, the STJ filter used on our tracking scheme in Bourdin et al  
1175 (2022) offers similar performances to the VTU method in terms of false alarms  
1176 but has the benefit of preserving the probability of detection, particularly in  
1177 the NATl basin. However, The VTU filter presents the interesting property of  
1178 being dependent only on the instantaneous and local state of the atmosphere  
1179 whereas the STJ filter requires the use of temporal smoothing over large scale  
1180 fields. This property of the VTU method makes it possible to implement this  
1181  
1182  
1183  
1184  
1185  
1186  
1187  
1188  
1189  
1190  
1191  
1192  
1193  
1194  
1195  
1196

criterion as an online diagnostic within a tracking algorithm rather than as a post-processing.

In Sections 3.2 to 3.4 we presented our results on the physical representation of TCs in the ERA5 reanalysis. These results highlighted the underestimation of TC induced wind speeds in ERA5. This underestimation is in fact not specific to ERA5 but concerns all reanalyses, even those (to a lesser extent) with the TC-specific assimilation techniques mentioned in Section 1, and cannot solely be explained by the coarse grid resolution of these products (Schenkel and Hart, 2012; Hodges et al, 2017; Zarzycki et al, 2021). Moreover, we note that the wind-pressure relationship measured in ERA5 (Figure 3) appears somewhat degraded compared to those found with two predecessors of ERA5: ERA-40 and ERA-Interim (Murakami, 2014; Hodges et al, 2017) due to the discrepancy in how well both the wind speeds and SLPs are represented in ERA5. Therefore — and while the exact origin of the underestimation remains unknown at this point — these elements could hint towards an issue with the model’s physics.

We also showed in Section 3.3 that TC intensification rate prior to peak intensity was greater in the best-track catalog than in ERA5, which is consistent with the results from Schenkel and Hart (2012) obtained on five reanalyses (including ERA-40 and ERA-Interim). However, we find that while all categories of ERA5 TCs reach their peak intensity later than in IBTrACS when looking at the mean lag, the first quartile for the TS and Cat 1 groups below 0 indicate that a considerable amount of TCs peak earlier than in IBTrACS in these categories. This distinction may be the result of differences in methodologies compared to Schenkel and Hart (2012), mainly with regard to the identification of the time of maximum intensity in IBTrACS, as discussed in

1243 Section 3.3, but could also partly result from the increase in horizontal reso-  
1244 lution in ERA5 compared to the reanalyses used in [Schenkel and Hart \(2012\)](#).  
1245 Nevertheless, this result is consistent with how ERA5 appears to represent low  
1246 intensity TCs better than those from higher categories.  
1247

1248 [Zick and Matyas \(2015\)](#) analyzed the internal structure of TCs in both the  
1249 North American Regional Reanalysis (NARR) and CFSR datasets by com-  
1250 puting the mean composited radial-height cross section over the ten most  
1251 intense TCs (according to the reanalyses) and highlighted key structural dif-  
1252 ferences between both. Interestingly, the temperature anomaly cross-section  
1253 in ERA5 (Figure 8) has similar features to that from NARR — namely, the  
1254 distinct upper-tropospheric peak and the secondary, weaker, mid-level warm-  
1255 ing — while the ERA5 tangential wind speed cross-section (Figure 7, right  
1256 panel) shares more similarity with that from CFSR with a vertical distribu-  
1257 tion of the maximum wind speed. As stated by [Zick and Matyas \(2015\)](#), this  
1258 vertical distribution of the tangential wind speed is consistent with observa-  
1259 tional studies based on dropwindsonde and Doppler radar data ([Franklin et al,](#)  
1260 [2003](#); [Stern and Nolan, 2011](#)). Furthermore, the positive correlation between  
1261 the altitude of the maximum temperature anomaly and TC intensity (Table  
1262 2) has also been documented by observational studies ([Zhang et al, 2015](#); [Gao](#)  
1263 [et al, 2017](#)). More recently, [Wang and Jiang \(2019\)](#) produced a 13-year cli-  
1264 matology of TC warm-core structures based on data from the Atmospheric  
1265 Infrared Sounder onboard the AQUA satellite, from which they derived typi-  
1266 cal warm-core heights for each SSHS intensity class. We find that compared to  
1267 the aforementioned study, the warm core in ERA5 do not rise as high, capping  
1268 at 300 hPa against 150 hPa for the observations. However, we acknowledge  
1269 that there is no consensus about the link between warm-core elevation and  
1270 TC intensity to this day ([Stern and Nolan, 2012](#)). Moreover, it is important to  
1271  
1272  
1273  
1274  
1275  
1276  
1277  
1278  
1279  
1280  
1281  
1282  
1283  
1284  
1285  
1286  
1287  
1288

remind the reader that the selected compositing times here are based on the  
observed intensity rather than on the reanalysis. Bearing in mind that the delay  
between the maximum intensity of ERA5 and IBTrACS TCs increases with  
IBTrACS TC intensity, it is possible that replicating this analysis according to  
the model's intensity would yield slightly different results. For instance, warm  
core elevation for Cat 4 and 5 could increase, and the decrease in intensity  
between Cat 3 and Cat 4 would also likely disappear. At any rate, the inability  
to distinguish TC intensity from their internal structure above Cat 3 in the  
averaged composites, combined with the large intensity spread associated with  
reanalyzed TCs within any given SSHS group adds as many extra sources of  
uncertainty for users wanting to study the internal structure of historical TCs.

Despite some discrepancies in the representation of TCs in ERA5, the  
reanalysis can still be a valuable tool for the study of tropical cyclones and  
is capable of producing substantially stronger TCs than ERA-I. It also offers  
good spatial and temporal homogeneity whereas the differences in detection  
procedure and maximum wind speed measurement techniques between the  
meteorological agencies that contribute to IBTrACS produce substantial heterogeneity  
within the best track catalog (Schreck et al, 2014; Hodges et al, 2017). This is of course to be nuanced by the fact that the quality of observations assimilated in ERA5 also improves with time (Bengtsson et al, 2004; Rienecker et al, 2012) and that not all regions have the same observational coverage. For instance, the Northern Hemisphere benefits from aircraft reconnaissance as well as from a large network of ground stations in addition to satellite observations, the latter being the primary data source in the Southern Hemisphere.

One could consider using bias correction techniques to alleviate bias in wind speed and minimum SLP values. This is however not trivial as most bias

1335 correction methods are rank-preserving (e.g. quantile-quantile) and we showed  
1336 with Figure 4 that the reanalysis does not preserve the observed rank of TCs.  
1337 One other strength of atmospheric reanalyses lies within the fact that they  
1338 allow not only to study the 3D variables associated within the TC itself (as  
1339 was showcased in this paper), but also the large scale environment in which  
1340 TCs occur. In both cases, being able to locate precisely TCs in the reanalysis  
1341 is essential as TC position between a reanalysis and IBTrACS rarely coincide  
1342 perfectly, hence the need for an objective TC tracking scheme. ERA5 continues  
1343 on the path of improvement, following in the footsteps of its predecessors, in  
1344 part due to its increased horizontal resolution, but TC representation would  
1345 undoubtedly benefit from the use of TC-specific treatments.  
1346  
1347  
1348  
1349  
1350  
1351  
1352  
1353  
1354  
1355  
1356  
1357  
1358  
1359  
1360  
1361  
1362  
1363  
1364  
1365  
1366  
1367  
1368  
1369  
1370  
1371  
1372  
1373  
1374  
1375  
1376  
1377  
1378  
1379  
1380

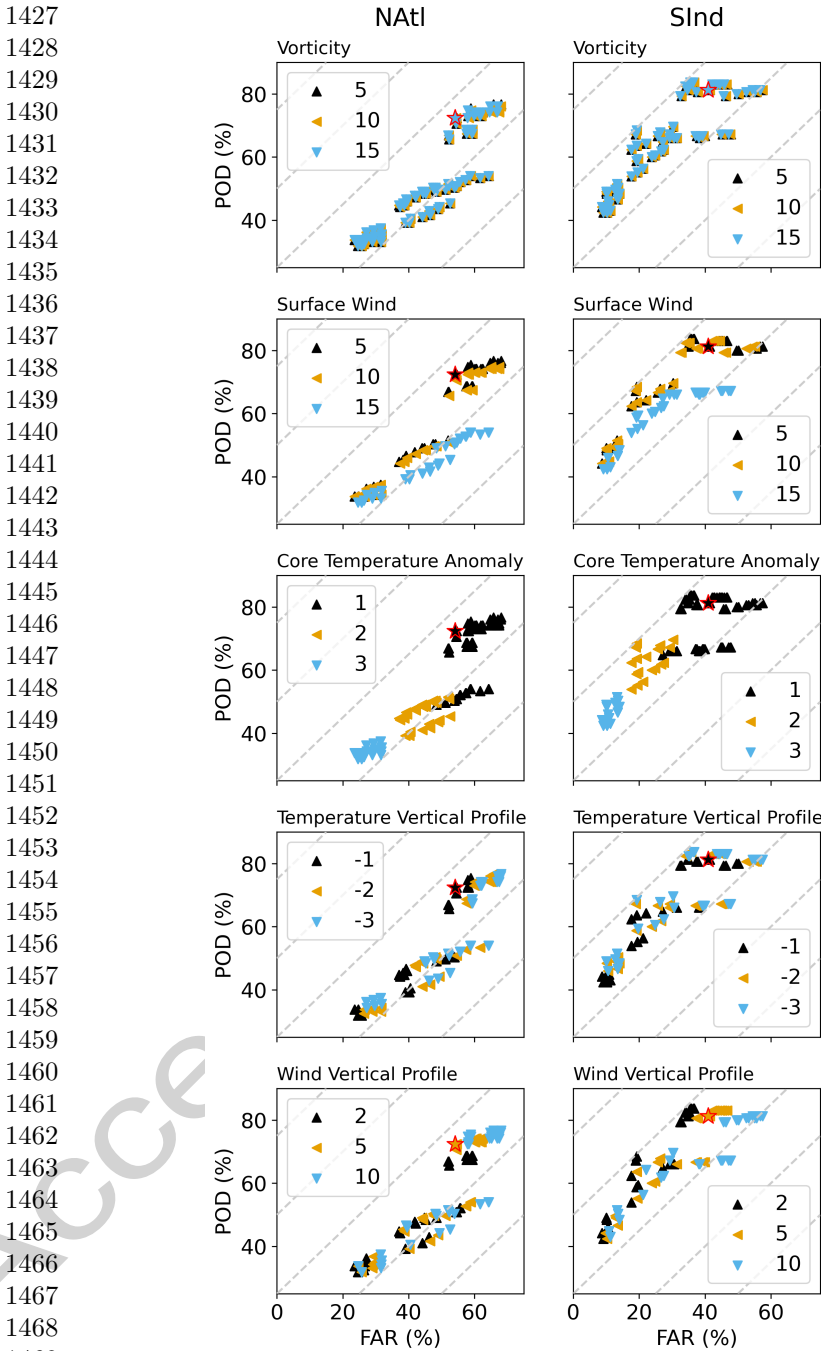


## Appendix A Tuning the tracker's detection thresholds

In this section we present a sensitivity analysis of the tracking scheme to its detection thresholds in order to identify a set of tracking parameters (see 2.2) that maximizes the efficiency of detection while limiting the amount of false alarms. In such cases where two or more objectives are to be simultaneously optimized, no single solution can be derived as there is a trade-off between the objectives. One can however aim to approach a solution that is said to be *Pareto efficient* if one of the objectives cannot be improved further without degrading the other (Zitzler and Thiele, 1999; Deb, 2011).

To find such a solution, we explore the parameters' space by perturbing the tracking parameters so that they can each take three different values, thus forming a set of 243 combinations of five thresholds, called vectors or solutions. The values of each parameters are presented in Table A1. For each vector, our tracking scheme is applied on both the North Atlantic (NA<sub>tl</sub>) region — which is the best observed basin — and the South Indian (SI<sub>nd</sub>) basin — which is under Météo-France forecasting responsibility — from season 2008 to 2018. We justify why the conclusions drawn from two basins can be largely be applied to other regions at the end of Section A. We then proceed to pair the detected tracks with IBTrACS, following the methodology from 2.3 and compute the FAR and POD integrated over the 11-year period.

Figure A1 presents each combination of thresholds in FAR / POD space for both basins, called the objective space. In the objective space, an ideal solution maximizing the POD while minimizing the FAR would be located in the upper left corner of the plots, i.e. POD=100 % and FAR=0 %. However such a solution does not exist here as FAR and POD appear to be related to each other through a non-linear relationship such that improving the POD



1470 **Fig. A1** Objective space representation of each combination of thresholds. The first column  
1471 shows the results for the NATl basin and the second column those for the SInd basin. Each  
1472 of the five rows correspond to a detection criterion. Each point (combination of thresholds,  
a.k.a vector) is colored according to the value taken by said criterion. In each panel, the  
red-bordered star denotes the selected vector.

**Table A1** Detection thresholds values tested for the sensitivity analysis. Combinations of these values form a set of  $3^5$  vectors. The boxed value in each row denotes the value that was selected for the corresponding parameter to conduct the complete ERA5 tracking.

Criterion	Tested Values		
<b>VOR</b>			
Vorticity threshold ( $10^{-5} s^{-1}$ )	5	10	<b>15</b>
<b>RES</b>			
Surface wind speed threshold ( $m.s^{-1}$ )	<b>5</b>	10	15
<b>TANOM</b>			
Temperature anomaly threshold (K)	<b>1</b>	2	3
<b>PT</b>			
Temperature vertical gradient (K)	<b>-1</b>	-2	-3
<b>PW</b>			
Wind speed vertical gradient ( $m.s^{-1}$ )	2	<b>5</b>	10

generally tends to degrade the FAR, and vice versa. In fact, points located along the leftmost of the scatter plots indicate the best trade-off between POD and FAR based on our sample. Choosing a solution among the ones presented here is therefore a subjective choice expressing a balance between detection efficiency and false alarms rate.

These plots also inform us on how each threshold affects the performance of the tracking scheme in terms of these two metrics. For the **VOR**, most vectors are stacked on top of each other, indicating that the vorticity threshold has little impact on the tracker's performance, or that the sampling on this criterion was not selective enough. However, and while the effect cannot be seen visually here, higher **VOR** value appears to be associated with a lower FAR for vectors with high PODs. Indeed, vectors with a POD greater than 70 % show a 1 % relative decrease in FAR with **VOR** set at  $15 \cdot 10^{-5} s^{-1}$  compared to  $5 \cdot 10^{-5} s^{-1}$  in the NATl basin, and a 1.3 % relative decrease for SInd. This tends to show that the vorticity threshold may act as a false alarm filter. However, increasing the **VOR** too much would inevitably lead to a loss in POD as weaker TCs would fail to meet the criterion. Therefore we considered that the gain from testing with higher values would have been marginal with respect to the cost of conducting new experiments. Moreover,

1473  
1474  
1475  
1476  
1477  
1478  
1479  
1480  
1481  
1482  
1483  
1484  
1485  
1486  
1487  
1488  
1489  
1490  
1491  
1492  
1493  
1494  
1495  
1496  
1497  
1498  
1499  
1500  
1501  
1502  
1503  
1504  
1505  
1506  
1507  
1508  
1509  
1510  
1511  
1512  
1513  
1514  
1515  
1516  
1517  
1518

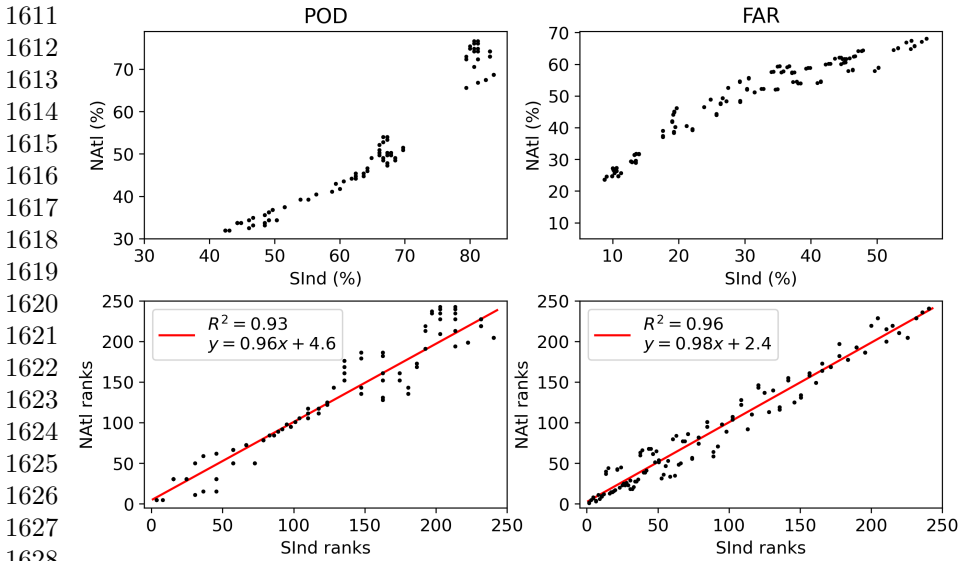
1519 the final set of tracks from the global tracking made with the threshold values  
1520 from Table A1 show a 0.1 % percentile of the maximum vorticity per matched  
1521 track of  $22 \cdot 10^{-5} \text{ s}^{-1}$  which tends to support this claim.  
1522  
1523  
1524 The surface wind speed threshold (**RES**) on the other hand has a clear impact  
1525 on performances as it effectively defines an upper bound for the POD. Setting  
1526 RES to  $15 \text{ m} \cdot \text{s}^{-1}$  bounds the POD to 54 % in NATl and 67.3 % in SInd. Bound-  
1527 aries formed by vectors with RES values set to 10 and  $5 \text{ m} \cdot \text{s}^{-1}$  are located  
1528 further up the POD axis and are capped respectively to 74.8 % and 76.7 % for  
1529 NATl and 83 % and 83.6 % for SInd. The sensitivity to the **RES** parameter  
1530 shows in fact that the POD saturates at RES=10, with RES=5 vectors offer-  
1531 ing only marginally better PODs in the NATl basin, and no apparent change in  
1532 the SInd basin. Because of the POD gap between RES=10 and RES=15, it is  
1533 possible that the saturation value is actually located between 10 and  $15 \text{ m} \cdot \text{s}^{-1}$ .  
1534  
1535  
1536 The temperature anomaly threshold (**TANOM**) stratifies the FAR as each  
1537 value taken by this parameter corresponds to a certain FAR range with little  
1538 overlapping. Reducing the threshold leads to an increased FAR, as it allows the  
1539 tracker to detect cooler systems. However, because of the link between FAR and  
1540 POD, an increased FAR generally implies a higher POD, making TANOM=1  
1541 vectors prime choices for finding a good performing solution within our set.  
1542  
1543  
1544 As for the last two detection thresholds that define the strength of vertical  
1545 profiles for respectively the temperature and horizontal wind speed (**PT** and  
1546 **PW**), they act by design as filters for extra-tropical cyclones — counting as  
1547 false alarms in our methodology — by ensuring the presence of respectively a  
1548 warmer upper core and stronger near-surface winds. Both of these properties  
1549 are indeed reversed in extra-tropical cyclones, and linked together by the ther-  
1550 mal wind relationship. No distinct pattern applicable to both regions and all  
1551 vectors emerge from the analysis. However, when considering only the group  
1552  
1553  
1554  
1555  
1556  
1557  
1558  
1559  
1560  
1561  
1562  
1563  
1564

of vectors with the highest POD in each region, increasing these thresholds 1565  
tends to deteriorate the FAR with marginal benefit to the POD. 1566  
1567

As a result, we chose VOR=15 for its potential to reduce the amount of 1568  
false alarms, RES=5 for the extended POD upper bound, TANOM=1 because 1569  
of the advantageous location of these vectors in the objective space for the 1570  
NAtl basin and selected a solution from the remaining candidates in our set 1571  
which we felt constituted a satisfying compromise in both regions — leaving 1572  
us with PT=1 and PW=5. The choice of a 5 m.s<sup>-1</sup> wind speed threshold and 1573  
its meaning for the CNRM TC Tracking Scheme is further discussed in the 1574  
Discussion section (Section 4). This particular solution exhibits a 54 % FAR 1575  
and 72.4 % POD in the NAtl region, and a 41 % FAR and 81.2 % POD in the 1576  
SInd basin. The important amount of false alarms in the chosen solution, the 1577  
majority of which being mid-latitude systems, motivated us to then add the 1578  
VTU post-processing method described in Section 2.2 as a mean of improving 1579  
performances even further. Applying the VTU method on the selected solution 1580  
brings down the FAR to respectively 15 % and 27 % for NAtl and SInd between 1581  
2008 and 2018. This reduction in FAR comes at a cost to the POD in the 1582  
NAtl basin which is lowered to 58 %. However, the POD in the SInd remains 1583  
unaffected by the use of the additional filter, which is likely due to the fact 1584  
that there is little TC activity at mid-latitudes in this region. 1585  
1586  
1587

Finally, it is worth noting that while our test vectors in the SInd region 1588  
present generally higher PODs in this experiment (14 points more in average) 1589  
and are arranged differently in the objective space than in the NAtl region, the 1590  
rankings of each vector on FAR and POD scales is approximately preserved 1591  
between both region, as can be seen in Figure A2 below. 1592  
1593  
1594  
1595  
1596  
1597

POD ranks between both basins indeed show a 0.96 correlation coefficient FAR 1598  
ranks are at 0.98, meaning that any given vector performs about as well in both 1599  
1600  
1601  
1602  
1603  
1604  
1605  
1606  
1607  
1608  
1609  
1610



1629 **Fig. A2** The left column places each vector POD-wise (upper left) and their respective  
 1630 ranks — from 1 to 243 — between both experiments (bottom left). The right column does  
 1631 the same FAR-wise. PODs are ranked in ascending order such that higher POD values have  
 1632 a higher rank and FARs in descending order. The red line on the bottom row panels show the  
 1633 fitted line between NATl and SInd ranks and exhibit a 0.97 and 0.94 correlation coefficient  
 1634 for POD and FAR, respectively.

1635 basins with respect to the other vectors. This gives us confidence in the fact  
 1636 that tuning our algorithm over two basins only can be relevant for all basins.

1637  
1638  
1639  
1640  
1641  
1642  
1643  
1644  
1645  
1646  
1647  
1648  
1649  
1650  
1651  
1652  
1653  
1654  
1655  
1656

Appendix B Supplementary figures

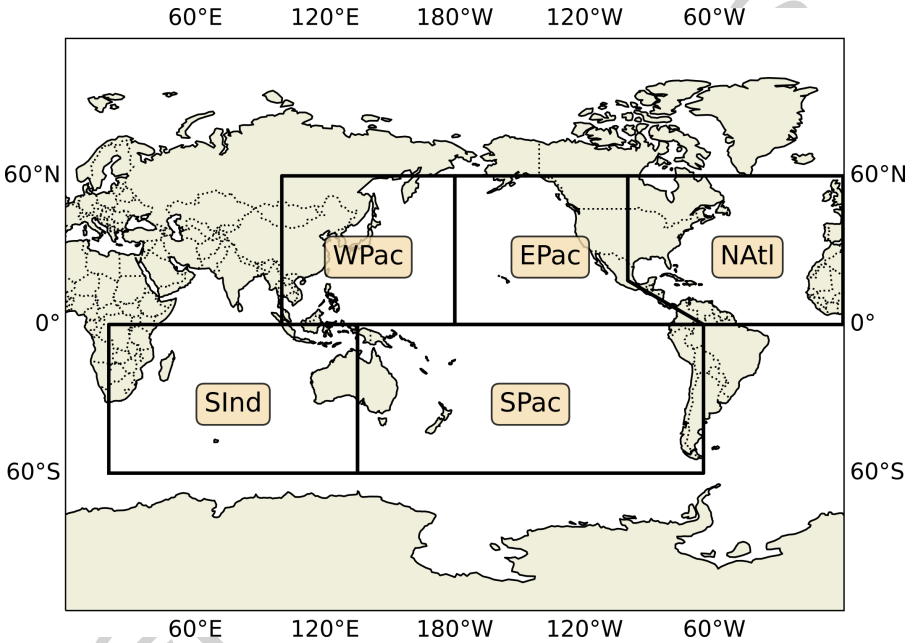
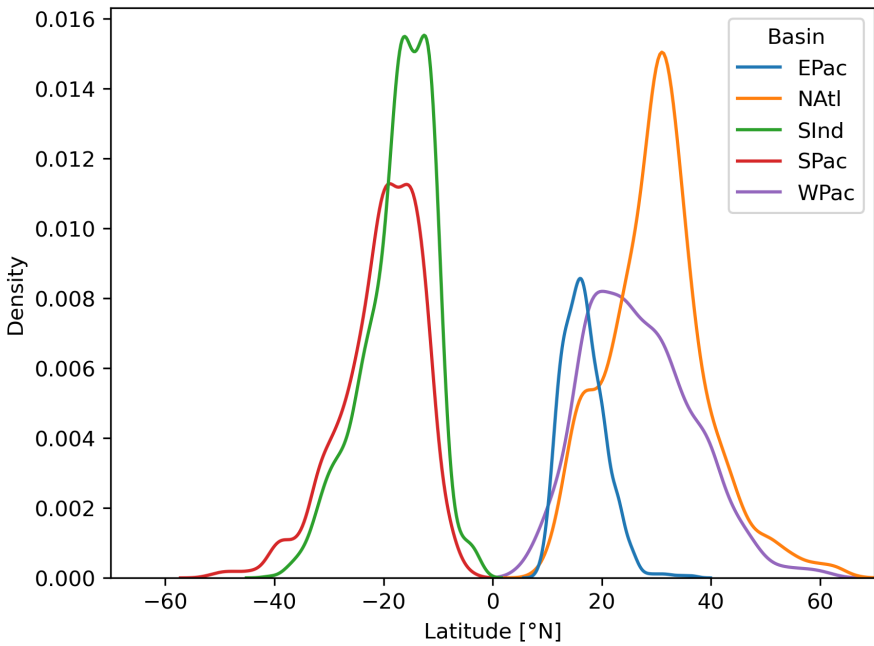


Fig. B3 Geographical basins definition. Adapted from Knutson et al (2020)

1657  
1658  
1659  
1660  
1661  
1662  
1663  
1664  
1665  
1666  
1667  
1668  
1669  
1670  
1671  
1672  
1673  
1674  
1675  
1676  
1677  
1678  
1679  
1680  
1681  
1682  
1683  
1684  
1685  
1686  
1687  
1688  
1689  
1690  
1691  
1692  
1693  
1694  
1695  
1696  
1697  
1698  
1699  
1700  
1701  
1702

1703  
 1704  
 1705  
 1706  
 1707  
 1708  
 1709  
 1710  
 1711  
 1712  
 1713  
 1714  
 1715  
 1716  
 1717  
 1718  
 1719  
 1720  
 1721  
 1722  
 1723  
 1724  
 1725  
 1726  
 1727  
 1728  
 1729  
 1730  
 1731  
 1732  
 1733  
 1734  
 1735  
 1736  
 1737  
 1738  
 1739  
 1740  
 1741  
 1742  
 1743  
 1744  
 1745  
 1746  
 1747  
 1748



**Fig. B4** Estimated PDFs of the latitudes of the IBTrACS systems matched with ERA5 tracks that are removed by the VTU post-processing for each basin of interest.



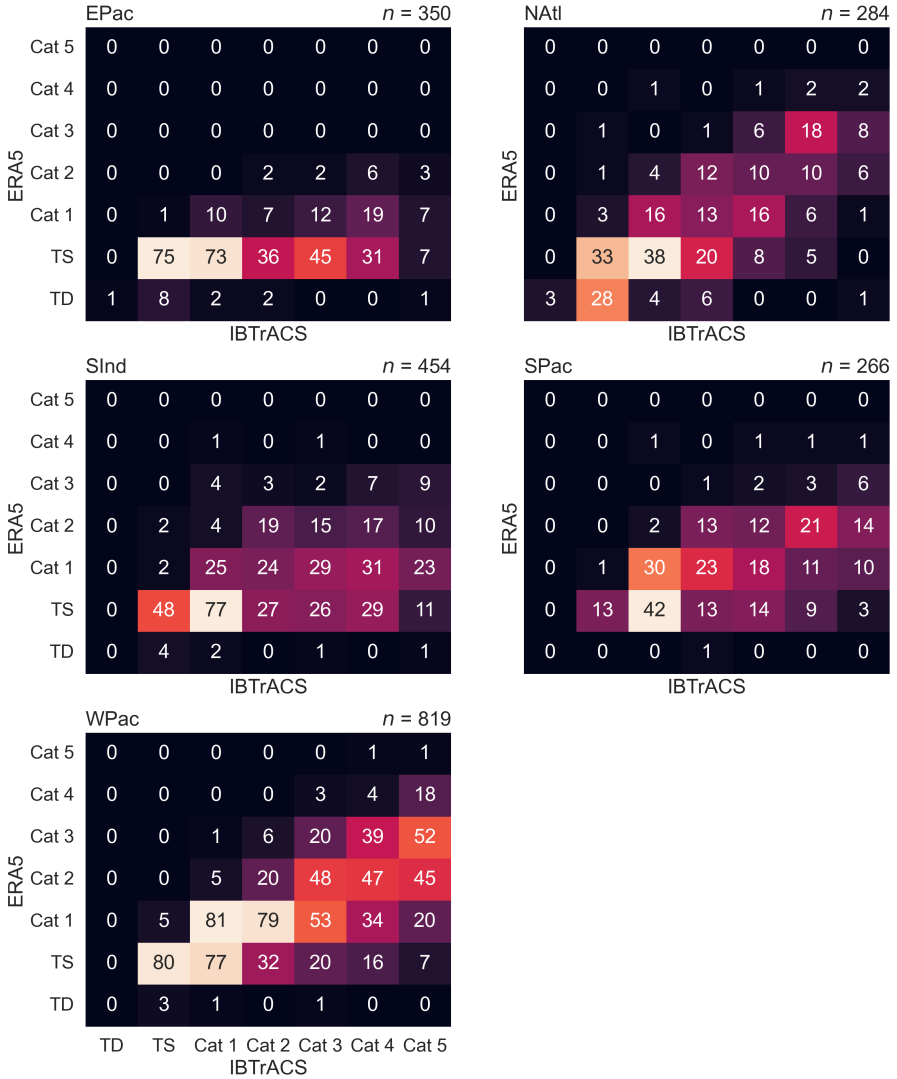


**Fig. B5** Per basin contingency crosstables between ERA5 and IBTrACS pressure-based intensity classes.

1749  
1750  
1751  
1752  
1753  
1754  
1755  
1756  
1757  
1758  
1759  
1760  
1761  
1762  
1763  
1764  
1765  
1766  
1767  
1768  
1769  
1770  
1771  
1772  
1773  
1774  
1775  
1776  
1777  
1778  
1779  
1780  
1781  
1782  
1783  
1784  
1785  
1786  
1787  
1788  
1789  
1790  
1791  
1792  
1793  
1794

1795  
 1796  
 1797  
 1798  
 1799  
 1800  
 1801  
 1802  
 1803  
 1804  
 1805  
 1806  
 1807  
 1808  
 1809  
 1810  
 1811  
 1812  
 1813  
 1814  
 1815  
 1816  
 1817  
 1818  
 1819  
 1820  
 1821  
 1822  
 1823  
 1824  
 1825  
 1826  
 1827  
 1828  
 1829  
 1830  
 1831  
 1832  
 1833  
 1834  
 1835  
 1836  
 1837  
 1838  
 1839  
 1840

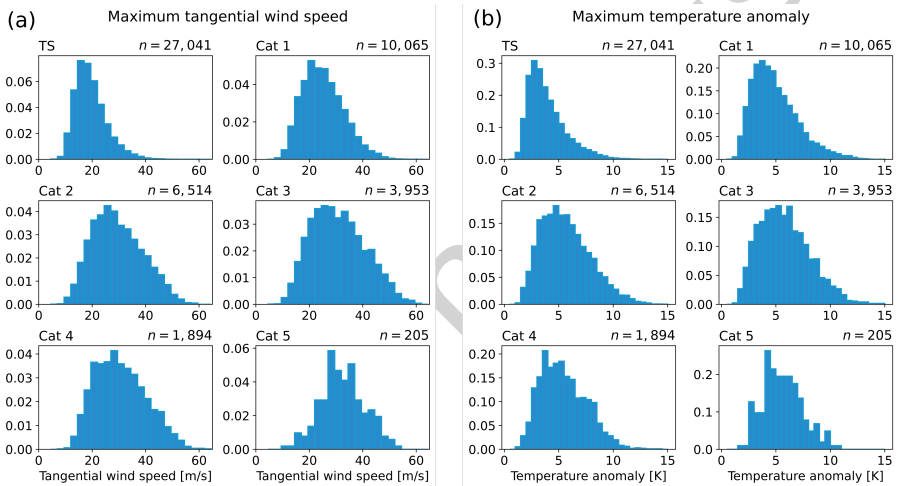


**Fig. B6** Distributions of (a) the maximum tangential wind speed per composed radius-height cross-section for each observed SSHWS intensity class, and for the maximum temperature anomaly (b).

<b>Declarations</b>	1841
	1842
	1843
<b>Funding</b>	1844
	1845
This work was partly supported by the French National program LEFE	1846
(Les Enveloppes Fluides et l'Environnement), specifically by the CYPRESSA	1847
project.	1848
	1849
	1850
	1851
<b>Competing interests</b>	1852
	1853
The authors have no relevant financial or non-financial interests to disclose.	1854
	1855
	1856
<b>Author contributions</b>	1857
	1858
WD carried out the study under the guidance of JC and FC. FC provided	1859
the tracking scheme. SB provided the VTU post-processing. WD did the	1860
figures and wrote the manuscript. All authors provided critical feedback and	1861
contributed to the revisions.	1862
	1863
	1864
	1865
	1866
<b>Data availability</b>	1867
	1868
The ERA5 data used was obtained from the ESPRI Mesocentre from the	1869
IPSL, Polytechnique, but is otherwise available through the Copernicus Cli-	1870
mate Change Service (C3S) Climate Data Store (CDS). The IBTrACS catalog	1871
is available at <a href="https://www.ncei.noaa.gov/products/international-best-track-archive">https://www.ncei.noaa.gov/products/international-best-track-</a>	1872
<a href="https://www.ncei.noaa.gov/products/international-best-track-archive">archive</a> . The tracking and track pairing data generated and analysed during	1873
the current study are available from the corresponding author on reasonable	1874
request.	1875
	1876
	1877
	1878
	1879
	1880
	1881
	1882
	1883
	1884
	1885
	1886

1887 **References**

1888

1889 Atkinson GD, Holliday CR (1977) Tropical Cyclone Minimum Sea  
18901891 Level Pressure/Maximum Sustained Wind Relationship for the  
1892 Western North Pacific. *Monthly Weather Review* 105(4):421–427.1893 [https://doi.org/10.1175/1520-0493\(1977\)105<0421:TCMSLP>2.0.CO;2](https://doi.org/10.1175/1520-0493(1977)105<0421:TCMSLP>2.0.CO;2),

1894

1895 URL [https://journals.ametsoc.org/view/journals/mwre/105/4/](https://journals.ametsoc.org/view/journals/mwre/105/4/1520-0493_1977_105_0421_tcmslp_2_0_co_2.xml)

1896

1897 [1520-0493\\_1977\\_105\\_0421\\_tcmslp\\_2\\_0\\_co\\_2.xml](https://journals.ametsoc.org/view/journals/mwre/105/4/1520-0493_1977_105_0421_tcmslp_2_0_co_2.xml), publisher: American

1898

1899 Meteorological Society Section: *Monthly Weather Review*

1900

1901

1902 Bell B, Hersbach H, Simmons A, et al (2021) The ERA5 global reanalysis:

1903

1904 Preliminary extension to 1950. *Quarterly Journal of the Royal Mete-*  
1905 *orological Society* 147(741):4186–4227. <https://doi.org/10.1002/qj.4174>,

1906

1907 URL <https://onlinelibrary.wiley.com/doi/abs/10.1002/qj.4174>, eprint:

1908

1909 <https://onlinelibrary.wiley.com/doi/pdf/10.1002/qj.4174>

1910

1911 Bell R, Strachan J, Vidale PL, et al (2013) Response of Tropical  
1912

1913 Cyclones to Idealized Climate Change Experiments in a Global High-

1914

1915 Resolution Coupled General Circulation Model. *Journal of Climate*  
1916 26(20):7966–7980. <https://doi.org/10.1175/JCLI-D-12-00749.1>, URL [https:](https://journals.ametsoc.org/view/journals/clim/26/20/jcli-d-12-00749.1.xml)

1917

1918 [//journals.ametsoc.org/view/journals/clim/26/20/jcli-d-12-00749.1.xml](https://journals.ametsoc.org/view/journals/clim/26/20/jcli-d-12-00749.1.xml),

1919

1920 publisher: American Meteorological Society Section: *Journal of Climate*

1921

1922 Bengtsson L, Hagemann S, Hodges KI (2004) Can climate trends be  
19231924 calculated from reanalysis data? *Journal of Geophysical Research:*  
1925 *Atmospheres* 109(D11). <https://doi.org/10.1029/2004JD004536>, URL

1926

1927 <https://onlinelibrary.wiley.com/doi/abs/10.1029/2004JD004536>, eprint:

1928

1929 <https://onlinelibrary.wiley.com/doi/pdf/10.1029/2004JD004536>

1930

1931

1932

- Bourdin S, Fromang S, Dulac W, et al (2022) Intercomparison of four algorithms for detecting tropical cyclones using ERA5. *Geoscientific Model Development* 15(17):6759–6786. <https://doi.org/10.5194/gmd-15-6759-2022>, URL <https://gmd.copernicus.org/articles/15/6759/2022/>, publisher: Copernicus GmbH
- Cesana G, Waliser DE, Jiang X, et al (2015) Multimodel evaluation of cloud phase transition using satellite and reanalysis data. *Journal of Geophysical Research: Atmospheres* 120(15):7871–7892. <https://doi.org/10.1002/2014JD022932>, URL <https://onlinelibrary.wiley.com/doi/abs/10.1002/2014JD022932>, eprint: <https://onlinelibrary.wiley.com/doi/pdf/10.1002/2014JD022932>
- Chauvin F, Royer JF, Déqué M (2006) Response of hurricane-type vortices to global warming as simulated by ARPEGE-Climat at high resolution. *Climate Dynamics* 27(4):377–399. <https://doi.org/10.1007/s00382-006-0135-7>, URL <http://link.springer.com/10.1007/s00382-006-0135-7>
- Davis CA (2018) Resolving Tropical Cyclone Intensity in Models. *Geophysical Research Letters* 45(4):2082–2087. <https://doi.org/https://doi.org/10.1002/2017GL076966>, URL <https://agupubs.onlinelibrary.wiley.com/doi/abs/10.1002/2017GL076966>, eprint: <https://agupubs.onlinelibrary.wiley.com/doi/pdf/10.1002/2017GL076966>
- Deb K (2011) Multi-objective Optimisation Using Evolutionary Algorithms: An Introduction. In: Wang L, Ng AHC, Deb K (eds) *Multi-objective Evolutionary Optimisation for Product Design and Manufacturing*. Springer, London, p 3–34, [https://doi.org/10.1007/978-0-85729-652-8\\_1](https://doi.org/10.1007/978-0-85729-652-8_1), URL [https://doi.org/10.1007/978-0-85729-652-8\\_1](https://doi.org/10.1007/978-0-85729-652-8_1)

- 1979 Dee DP, Uppala SM, Simmons AJ, et al (2011) The ERA-Interim reanalysis:  
1980 configuration and performance of the data assimilation system. Quarterly  
1981 Journal of the Royal Meteorological Society 137(656):553–597. <https://doi.org/10.1002/qj.828>, URL <https://onlinelibrary.wiley.com/doi/abs/10.1002/qj.828>,  
1982 <https://onlinelibrary.wiley.com/doi/pdf/10.1002/qj.828>  
1983 [\\_eprint: https://onlinelibrary.wiley.com/doi/pdf/10.1002/qj.828](https://onlinelibrary.wiley.com/doi/pdf/10.1002/qj.828)  
1984  
1985  
1986  
1987
- 1988 Ebita A, Kobayashi S, Ota Y, et al (2011) The Japanese 55-year Reanaly-  
1989 sis “JRA-55”: An Interim Report. *Sola* 7:149–152. <https://doi.org/10.2151/sola.2011-038>  
1990  
1991  
1992  
1993
- 1994 Fasullo JT (2020) Evaluating simulated climate patterns from the CMIP  
1995 archives using satellite and reanalysis datasets using the Climate  
1996 Model Assessment Tool (CMATv1). *Geoscientific Model Development*  
1997 13(8):3627–3642. <https://doi.org/10.5194/gmd-13-3627-2020>, URL <https://gmd.copernicus.org/articles/13/3627/2020/>, publisher: Copernicus GmbH  
1998  
1999  
2000  
2001  
2002
- 2003 Franklin JL, Black ML, Valde K (2003) GPS Dropwindsonde Wind Profiles  
2004 in Hurricanes and Their Operational Implications. *Weather and Fore-  
2005 casting* 18(1):32–44. [https://doi.org/10.1175/1520-0434\(2003\)018<0032:  
2006 GDWPIH>2.0.CO;2](https://doi.org/10.1175/1520-0434(2003)018<0032:GDWPIH>2.0.CO;2), URL [https://journals.ametsoc.org/view/journals/  
2007 wefo/18/1/1520-0434\\_2003\\_018\\_0032\\_gdwpih\\_2\\_0\\_co\\_2.xml](https://journals.ametsoc.org/view/journals/wefo/18/1/1520-0434_2003_018_0032_gdwpih_2_0_co_2.xml), publisher:  
2008 American Meteorological Society Section: Weather and Forecasting  
2009  
2010  
2011  
2012  
2013
- 2014 Gao S, Chen B, Li T, et al (2017) AIRS-observed warm core structures of trop-  
2015 ical cyclones over the western North Pacific. *Dynamics of Atmospheres and  
2016 Oceans* 77:100–106. <https://doi.org/10.1016/j.dynatmoce.2016.12.001>, URL  
2017 <https://www.sciencedirect.com/science/article/pii/S037702651630104X>  
2018  
2019  
2020
- 2021 Gelaro R, McCarty W, Suárez MJ, et al (2017) The Modern-  
2022 Era Retrospective Analysis for Research and Applications, Version 2  
2023  
2024

- (MERRA-2). *Journal of Climate* 30(14):5419–5454. <https://doi.org/10.1175/JCLI-D-16-0758.1>, URL <https://journals.ametsoc.org/view/journals/clim/30/14/jcli-d-16-0758.1.xml>, publisher: American Meteorological Society Section: *Journal of Climate*
- Hart RE (2003) A Cyclone Phase Space Derived from Thermal Wind and Thermal Asymmetry. *Monthly Weather Review* 131(4):585–616. [https://doi.org/10.1175/1520-0493\(2003\)131<0585:ACPSDF>2.0.CO;2](https://doi.org/10.1175/1520-0493(2003)131<0585:ACPSDF>2.0.CO;2), URL [https://journals.ametsoc.org/view/journals/mwre/131/4/1520-0493\\_2003\\_131\\_0585\\_acpsdf\\_2.0.co.2.xml](https://journals.ametsoc.org/view/journals/mwre/131/4/1520-0493_2003_131_0585_acpsdf_2.0.co.2.xml), publisher: American Meteorological Society Section: *Monthly Weather Review*
- Hatsushika H, Tsutsui J, Fiorino M, et al (2006) Impact of Wind Profile Retrievals on the Analysis of Tropical Cyclones in the JRA-25 Reanalysis. *Journal of the Meteorological Society of Japan Ser II* 84(5):891–905. <https://doi.org/10.2151/jmsj.84.891>
- Hersbach H, Bell B, Berrisford P, et al (2020) The ERA5 global reanalysis. *Quarterly Journal of the Royal Meteorological Society* 146(730):1999–2049. <https://doi.org/10.1002/qj.3803>, URL <https://onlinelibrary.wiley.com/doi/abs/10.1002/qj.3803>, eprint: <https://onlinelibrary.wiley.com/doi/pdf/10.1002/qj.3803>
- Hodges K, Cobb A, Vidale PL (2017) How Well Are Tropical Cyclones Represented in Reanalysis Datasets? *Journal of Climate* 30(14):5243–5264. <https://doi.org/10.1175/JCLI-D-16-0557.1>, URL <https://journals.ametsoc.org/view/journals/clim/30/14/jcli-d-16-0557.1.xml>, publisher: American Meteorological Society Section: *Journal of Climate*

- 2071 Hodges KI (1994) A General Method for Tracking Analysis and Its Applica-  
2072 tion to Meteorological Data. *Monthly Weather Review* 122(11):2573–2586.  
2073 [https://doi.org/10.1175/1520-0493\(1994\)122<2573:AGMFTA>2.0.CO;2](https://doi.org/10.1175/1520-0493(1994)122<2573:AGMFTA>2.0.CO;2),  
2074 URL [https://journals.ametsoc.org/view/journals/mwre/122/11/  
2075 1520-0493\\_1994\\_122\\_2573\\_agmfta\\_2\\_0\\_co\\_2.xml](https://journals.ametsoc.org/view/journals/mwre/122/11/1520-0493_1994_122_2573_agmfta_2_0_co_2.xml), publisher: American  
2076 Meteorological Society Section: *Monthly Weather Review*  
2077  
2078  
2079  
2080  
2081  
2082 Kalnay E, Kanamitsu M, Kistler R, et al (1996) The NCEP/NCAR 40-  
2083 Year Reanalysis Project. *Bulletin of the American Meteorological Society*  
2084 77(3):437–472. [https://doi.org/10.1175/1520-0477\(1996\)077<0437:TNYRP>  
2085 2.0.CO;2](https://doi.org/10.1175/1520-0477(1996)077<0437:TNYRP>2.0.CO;2), URL [https://journals.ametsoc.org/view/journals/bams/77/3/  
2086 1520-0477\\_1996\\_077\\_0437\\_tnyrp\\_2\\_0\\_co\\_2.xml](https://journals.ametsoc.org/view/journals/bams/77/3/1520-0477_1996_077_0437_tnyrp_2_0_co_2.xml), publisher: American Meteo-  
2087 rological Society Section: *Bulletin of the American Meteorological Society*  
2088  
2089  
2090  
2091  
2092  
2093 Klotzbach PJ, Bell MM, Bowen SG, et al (2020) Surface Pressure a More Skill-  
2094 ful Predictor of Normalized Hurricane Damage than Maximum Sustained  
2095 Wind. *Bulletin of the American Meteorological Society* 101(6):E830–  
2096 E846. <https://doi.org/10.1175/BAMS-D-19-0062.1>, URL <https://journals.ametsoc.org/view/journals/bams/101/6/bamsD190062.xml>,  
2097 publisher: American Meteorological Society Section: *Bulletin of the*  
2098  
2099  
2100  
2101  
2102  
2103  
2104  
2105 Knapp KR, Kruk MC, Levinson DH, et al (2010) The International Best Track  
2106 Archive for Climate Stewardship (IBTrACS): Unifying Tropical Cyclone  
2107 Data. *Bulletin of the American Meteorological Society* 91(3):363–376.  
2108 <https://doi.org/10.1175/2009BAMS2755.1>, URL [https://journals.ametsoc.  
2109 org/view/journals/bams/91/3/2009bams2755\\_1.xml](https://journals.ametsoc.org/view/journals/bams/91/3/2009bams2755_1.xml), publisher: American  
2110 Meteorological Society Section: *Bulletin of the American Meteorological*  
2111  
2112  
2113  
2114  
2115  
2116



- Knutson T, Camargo SJ, Chan JCL, et al (2020) Tropical Cyclones and Climate Change Assessment: Part II: Projected Response to Anthropogenic Warming. *Bulletin of the American Meteorological Society* 101(3):E303–E322. <https://doi.org/10.1175/BAMS-D-18-0194.1>, URL <https://journals.ametsoc.org/view/journals/bams/101/3/bams-d-18-0194.1.xml>, publisher: American Meteorological Society Section: Bulletin of the American Meteorological Society 2117–2128
- Murakami H (2014) Tropical cyclones in reanalysis data sets. *Geophysical Research Letters* 41(6):2133–2141. <https://doi.org/10.1002/2014GL059519>, URL <https://onlinelibrary.wiley.com/doi/abs/10.1002/2014GL059519>, eprint: <https://onlinelibrary.wiley.com/doi/pdf/10.1002/2014GL059519> 2129–2136
- Murakami H, Sugi M (2010) Effect of Model Resolution on Tropical Cyclone Climate Projections. *Sola* 6:73–76. <https://doi.org/10.2151/sola.2010-019> 2137–2140
- Onogi K, Tsutsui J, Koide H, et al (2007) The JRA-25 Reanalysis. *Journal of the Meteorological Society of Japan Ser II* 85(3):369–432. <https://doi.org/10.2151/jmsj.85.369> 2141–2146
- Rathmann NM, Yang S, Kaas E (2014) Tropical cyclones in enhanced resolution CMIP5 experiments. *Climate Dynamics* 42(3):665–681. <https://doi.org/10.1007/s00382-013-1818-5>, URL <https://doi.org/10.1007/s00382-013-1818-5> 2147–2152
- Rienecker MM, Dee D, Woollen J, et al (2012) Atmospheric Reanalyses—Recent Progress and Prospects for the Future. A Report from a Technical Workshop, April 2010. Tech. Rep. GSFC.TM.6867.2012, NASA, URL <https://ntrs.nasa.gov/citations/20120014167>, nTRS Author Affiliations: NASA Goddard Space Flight Center, European Centre for Medium-Range Weather 2153–2162

- 2163 Forecasts, I M Systems Group, Colorado Univ., Japan Meteorological  
2164 Agency, Met Office (Meteorological Office), National Oceanic and Atmo-  
2165 spheric Administration NTRS Document ID: 20120014167 NTRS Research  
2166 Center: Goddard Space Flight Center (GSFC)  
2167  
2168  
2169
- 2170 Saha S, Moorthi S, Wu X, et al (2014) The NCEP Climate Fore-  
2171 cast System Version 2. *Journal of Climate* 27(6):2185–2208. <https://doi.org/10.1175/JCLI-D-12-00823.1>, URL <https://journals.ametsoc.org/view/journals/clim/27/6/jcli-d-12-00823.1.xml>, publisher: American Meteorolog-  
2172 ical Society Section: *Journal of Climate*  
2173  
2174  
2175  
2176  
2177  
2178
- 2179 Schenkel BA, Hart RE (2012) An Examination of Tropical Cyclone Posi-  
2180 tion, Intensity, and Intensity Life Cycle within Atmospheric Reanaly-  
2181 sis Datasets. *Journal of Climate* 25(10):3453–3475. <https://doi.org/10.1175/2011JCLI4208.1>, URL <https://journals.ametsoc.org/view/journals/clim/25/10/2011jcli4208.1.xml>, publisher: American Meteorological Society  
2182 Section: *Journal of Climate*  
2183  
2184  
2185  
2186  
2187  
2188
- 2189 Schreck CJ, Knapp KR, Kossin JP (2014) The Impact of Best  
2190 Track Discrepancies on Global Tropical Cyclone Climatologies using  
2191 IBTrACS. *Monthly Weather Review* 142(10):3881–3899. <https://doi.org/10.1175/MWR-D-14-00021.1>, URL <https://journals.ametsoc.org/view/journals/mwre/142/10/mwr-d-14-00021.1.xml>, publisher: American Meteo-  
2192 rological Society Section: *Monthly Weather Review*  
2193  
2194  
2195  
2196  
2197  
2198  
2199
- 2200  
2201 Stern DP, Nolan DS (2011) On the Vertical Decay Rate of the Max-  
2202 imum Tangential Winds in Tropical Cyclones. *Journal of the Atmo-  
2203 spheric Sciences* 68(9):2073–2094. <https://doi.org/10.1175/2011JAS3682.1>,  
2204 URL <https://journals.ametsoc.org/view/journals/atsc/68/9/2011jas3682.1>.  
2205  
2206  
2207  
2208

- [xml](#), publisher: American Meteorological Society Section: Journal of the Atmospheric Sciences 2209  
2210  
2211  
2212
- Stern DP, Nolan DS (2012) On the Height of the Warm Core in Tropical Cyclones. *Journal of the Atmospheric Sciences* 69(5):1657–1680. <https://doi.org/10.1175/JAS-D-11-010.1>, URL <https://journals.ametsoc.org/view/journals/atsc/69/5/jas-d-11-010.1.xml>, publisher: American Meteorological Society Section: Journal of the Atmospheric Sciences 2213  
2214  
2215  
2216  
2217  
2218  
2219  
2220  
2221
- Tiwari G, Kumar P (2022) Predictive skill comparative assessment of WRF 4DVar and 3DVar data assimilation: An Indian Ocean tropical cyclone case study. *Atmospheric Research* 277:106,288. <https://doi.org/10.1016/j.atmosres.2022.106288>, URL <https://www.sciencedirect.com/science/article/pii/S0169809522002745> 2222  
2223  
2224  
2225  
2226  
2227  
2228  
2229  
2230
- Tory KJ, Chand SS, Dare RA, et al (2013) The Development and Assessment of a Model-, Grid-, and Basin-Independent Tropical Cyclone Detection Scheme. *Journal of Climate* 26(15):5493–5507. <https://doi.org/10.1175/JCLI-D-12-00510.1>, URL <https://journals.ametsoc.org/view/journals/clim/26/15/jcli-d-12-00510.1.xml>, publisher: American Meteorological Society Section: Journal of Climate 2231  
2232  
2233  
2234  
2235  
2236  
2237  
2238  
2239  
2240  
2241
- Ullrich PA, Zarzycki CM (2017) TempestExtremes: a framework for scale-insensitive pointwise feature tracking on unstructured grids. *Geoscientific Model Development* 10(3):1069–1090. <https://doi.org/10.5194/gmd-10-1069-2017>, URL <https://gmd.copernicus.org/articles/10/1069/2017/>, publisher: Copernicus GmbH 2242  
2243  
2244  
2245  
2246  
2247  
2248  
2249  
2250  
2251  
2252  
2253  
2254

- 2255 Ullrich PA, Zarzycki CM, McClenny EE, et al (2021) TempestExtremes  
2256 v2.1: a community framework for feature detection, tracking, and anal-  
2257 ysis in large datasets. *Geoscientific Model Development* 14(8):5023–5048.  
2258 <https://doi.org/10.5194/gmd-14-5023-2021>, URL <https://gmd.copernicus.org/articles/14/5023/2021/>, publisher: Copernicus GmbH  
2262  
2263
- 2264 Uppala SM, Kållberg PW, Simmons AJ, et al (2005) The ERA-40  
2265 re-analysis. *Quarterly Journal of the Royal Meteorological Soci-*  
2266 *ety* 131(612):2961–3012. <https://doi.org/10.1256/qj.04.176>, URL  
2267 <https://onlinelibrary.wiley.com/doi/abs/10.1256/qj.04.176>, eprint:  
2268 <https://onlinelibrary.wiley.com/doi/pdf/10.1256/qj.04.176>  
2270  
2271
- 2272
- 2273 Voldoire A, Saint-Martin D, Sénési S, et al (2019) Evaluation of CMIP6  
2274 DECK Experiments With CNRM-CM6-1. *Journal of Advances in Modeling*  
2275 *Earth Systems* 11(7):2177–2213. <https://doi.org/10.1029/2019MS001683>,  
2276 URL <https://onlinelibrary.wiley.com/doi/abs/10.1029/2019MS001683>,  
2277 eprint: <https://onlinelibrary.wiley.com/doi/pdf/10.1029/2019MS001683>  
2280  
2281
- 2282 Walsh KJE, Fiorino M, Landsea CW, et al (2007) Objectively Deter-  
2283 mined Resolution-Dependent Threshold Criteria for the Detection of  
2284 Tropical Cyclones in Climate Models and Reanalyses. *Journal of Cli-*  
2285 *mate* 20(10):2307–2314. <https://doi.org/10.1175/JCLI4074.1>, URL <https://journals.ametsoc.org/view/journals/clim/20/10/jcli4074.1.xml>, publisher:  
2286  
2287  
2288  
2289  
2290  
2291  
2292
- 2293 Wang X, Jiang H (2019) A 13-Year Global Climatology of Tropical Cyclone  
2294 Warm-Core Structures from AIRS Data. *Monthly Weather Review*  
2295 147(3):773–790. <https://doi.org/10.1175/MWR-D-18-0276.1>, URL <https://journals.ametsoc.org/view/journals/mwre/147/3/mwr-d-18-0276.1.xml>,  
2296  
2297  
2298  
2299  
2300

publisher: American Meteorological Society Section: Monthly Weather Review	2301 2302 2303 2304
Whitaker JS, Compo GP, Thépaut JN (2009) A Comparison of Variational and Ensemble-Based Data Assimilation Systems for Reanalysis of Sparse Observations. <i>Monthly Weather Review</i> 137(6):1991–1999. <a href="https://doi.org/10.1175/2008MWR2781.1">https://doi.org/10.1175/2008MWR2781.1</a> , URL <a href="https://journals.ametsoc.org/view/journals/mwre/137/6/2008mwr2781.1.xml">https://journals.ametsoc.org/view/journals/mwre/137/6/2008mwr2781.1.xml</a> , publisher: American Meteorological Society Section: Monthly Weather Review	2305 2306 2307 2308 2309 2310 2311 2312 2313 2314 2315
Willoughby HE (1990) Gradient Balance in Tropical Cyclones. <i>Journal of the Atmospheric Sciences</i> 47(2):265–274. <a href="https://doi.org/10.1175/1520-0469(1990)047&lt;0265:GBITC&gt;2.0.CO;2">https://doi.org/10.1175/1520-0469(1990)047&lt;0265:GBITC&gt;2.0.CO;2</a> , URL <a href="https://journals.ametsoc.org/view/journals/atsc/47/2/1520-0469_1990_047_0265_gbitc_2_0_co_2.xml">https://journals.ametsoc.org/view/journals/atsc/47/2/1520-0469_1990_047_0265_gbitc_2_0_co_2.xml</a> , publisher: American Meteorological Society Section: Journal of the Atmospheric Sciences	2316 2317 2318 2319 2320 2321 2322 2323 2324 2325
Zarzycki CM, Ullrich PA, Reed KA (2021) Metrics for Evaluating Tropical Cyclones in Climate Data. <i>Journal of Applied Meteorology and Climatology</i> 60(5):643–660. <a href="https://doi.org/10.1175/JAMC-D-20-0149.1">https://doi.org/10.1175/JAMC-D-20-0149.1</a> , URL <a href="https://journals.ametsoc.org/view/journals/apme/60/5/JAMC-D-20-0149.1.xml">https://journals.ametsoc.org/view/journals/apme/60/5/JAMC-D-20-0149.1.xml</a> , publisher: American Meteorological Society Section: Journal of Applied Meteorology and Climatology	2327 2328 2329 2330 2331 2332 2333 2334 2335 2336
Zhang JA, Nolan DS, Rogers RF, et al (2015) Evaluating the Impact of Improvements in the Boundary Layer Parameterization on Hurricane Intensity and Structure Forecasts in HWRF. <i>Monthly Weather Review</i> 143(8):3136–3155. <a href="https://doi.org/10.1175/MWR-D-14-00339.1">https://doi.org/10.1175/MWR-D-14-00339.1</a> , URL <a href="https://journals.ametsoc.org/view/journals/mwre/143/8/mwr-d-14-00339">https://journals.ametsoc.org/view/journals/mwre/143/8/mwr-d-14-00339</a> .	2337 2338 2339 2340 2341 2342 2343 2344 2345 2346

2347 [1.xml](#), publisher: American Meteorological Society Section: Monthly  
2348 Weather Review  
2349  
2350  
2351 Zick SE, Matyas CJ (2015) Tropical cyclones in the North Ameri-  
2352 can Regional Reanalysis: An assessment of spatial biases in location,  
2353 intensity, and structure. *Journal of Geophysical Research: Atmo-*  
2354 *spheres* 120(5):1651–1669. <https://doi.org/10.1002/2014JD022417>, URL  
2355 <https://onlinelibrary.wiley.com/doi/abs/10.1002/2014JD022417>, eprint:  
2356 <https://onlinelibrary.wiley.com/doi/pdf/10.1002/2014JD022417>  
2357  
2358  
2359  
2360  
2361  
2362 Zitzler E, Thiele L (1999) Multiobjective evolutionary algorithms: a com-  
2363 parative case study and the strength Pareto approach. *IEEE Transactions*  
2364 *on Evolutionary Computation* 3(4):257–271. [https://doi.org/10.1109/4235.](https://doi.org/10.1109/4235.797969)  
2365 [797969](https://doi.org/10.1109/4235.797969), URL <http://ieeexplore.ieee.org/document/797969/>  
2366  
2367  
2368  
2369  
2370  
2371  
2372  
2373  
2374  
2375  
2376  
2377  
2378  
2379  
2380  
2381  
2382  
2383  
2384  
2385  
2386  
2387  
2388  
2389  
2390  
2391  
2392